Department of Physics and Astronomy
University of Heidelberg

Diploma thesis
in Physics
submitted by
Andreas Dörr
born in Filderstadt
2011

Setup, test and optimization of detection electronics for high-precision mass measurements at PENTATRAP

This diploma thesis has been carried out by Andreas Dörr
at the
Max-Planck-Institut für Kernphysik, Heidelberg
under the supervision of
Herrn Prof. Dr. Klaus Blaum

Aufbau, Test und Optimierung von Nachweiselektronik für hochpräzise Massenmessungen an PENTATRAP: Am Max-Planck-Institut für Kernphysik in Heidelberg befindet sich momentan das Hochpräzisions-Penningfallen-Massenspektrometer PENTATRAP im Aufbau. Das Experiment wird den Bereich hochpräziser Massenmessungen mit Unsicherheiten von der Größenordnung 0.01 ppb von den leichten Elementen in die Region der Elemente mittlerer und hoher Ordnungszahlen erweitern. PENTATRAP wird mit Massenmessungen dieser Genauigkeit beispielsweise zur Bestimmung der Ruhemasse des Elektron-Antineutrinos beitragen. Um die Masse der Ionen von Interesse zu messen werden die Bewegungsfrequenzen eines jeweils einzelnen in einer Penningfalle gespeicherten Ions bestimmt. Die Bestimmung erfolgt dabei über den Nachweis oszillierender Spiegelströme, welche die Bewegung des Ions in einem Nachweiskreis induziert. Diese Ströme liegen üblicherweise in der Größenordnung von fA. Deshalb muss die Nachweiselektronik äußerst empfindlich und rauscharm sein. Für die Nachweiseinheit zur Bestimmung der sogenannten Axialfrequenz, welche eine zentrale Rolle für hochpräzise Massenmessungen einnimmt, wurde im Rahmen dieser Arbeit ein Abwärtsmischer mit integrierter Seitenbandunterdrückung und einem rauscharmen Vorverstärker aufgebaut, getestet und optimiert. Zudem wurden erste Schritte unternommen, um einen rauscharmen auf einem SQUID basierenden Verstärker in den Aufbau des PENTATRAP-Experiments zu integrieren.

Setup, test and optimization of detection electronics for high-precision mass measurements at PENTATRAP: Currently, the high-precision Penning trap mass spectrometer PENTATRAP is being built at the Max-Planck-Institut für Kernphysik, Heidelberg. The experiment will extend the range of high-precision mass measurements with uncertainties on the order of 0.01 ppb from light elements to elements of medium and high atomic numbers. With mass measurements of this accuracy, PENTATRAP will contribute, e.g., to the determination of the electron anti-neutrino rest mass. To obtain the mass of an ion species of interest, motional frequencies of a single ion confined in a Penning trap are determined via the detection of oscillating image currents induced in detection circuits by the ion's motion. These currents are usually on the order of fA. Therefore, highly sensitive low-noise detection electronics is required. As a part of the detection unit for the determination of the so-called axial frequency, which plays a crucial role in high-precision mass measurements, a down converter with integrated sideband suppression and low-noise pre-amplifier was set up, tested and optimized within this thesis. Furthermore, first steps towards the integration of a low-noise SQUID based amplifier into the PENTATRAP setup were taken.

Erklärung:

Ich versichere, dass ich diese Arbeit selbstständig verfasst habe und keine anderen als die angegebenen Quellen und Hilfsmittel benutzt habe.

Heidelberg, den 06.06.2011 _____

Contents

List of Figures

List of Tables

List of Abbreviations

ADC	Analog-to-digital converter
DC	Direct current
EBIT	Electron Beam Ion Trap
FET	Field-effect transistor
FFT	Fast Fourier transform
FLL	Flux locked loop
HTS	High-temperature superconductor
IC	Integrated circuit
IF	Intermediate frequency
LNA	Low-noise amplifier
LO	Local oscillator
LTS	Low-temperature superconductor
PPF	Passive polyphase filter
RCSJ	Resistively and capacitively shunted junction
RF	Radio frequency
RSJ	Resistively shunted junction
SMD	Surface-mounted devices
SNR	Signal-to-noise ratio
SQUID	Superconducting quantum interference device
SSR	Sideband suppression ratio
TOF-ICR	Time-of-flight ion cyclotron resonance

1. Introduction

According to Einstein's famous relation $E = mc^2$, the mass reflects the whole energy content of a particle. Therefore, the mass of an atom is not just the sum of its electrons', protons' and neutrons' masses. It also contains atomic and nuclear binding energies. Thus, mass measurements allow to probe interactions within the atom. A review on mass measurement techniques and their applications in various fields of modern physics can be found in [Bla06].

Since the early days of mass spectrometry, mass measurements were carried out with charged particles in electric and magnetic fields [Tho97, Tho07]. To date, the most precise mass measurements have been performed with charged particles confined in the superposition of a strong homogeneous magnetic field $\vec{B}$ and a weak electrostatic potential Φ_e. This assembly is called Penning trap [Deh68, BG86]. The mass of a particle in a Penning trap is determined via the measurement of its cyclotron frequency $\omega_c = qB/m$, where q/m is the charge-to-mass ratio of the particle. With Penning traps, mass measurements have been carried out with uncertainties on the order of 10^{-11}. For example, Van Dyck et al. determined the mass of ^{4}He with an uncertainty of $1.6{\cdot}10^{-11}$ [VZV+04], or Redshaw et al. achieved an uncertainty of $2.1{\cdot}10^{-11}$ in their determination of the ^{28}Si mass [RMM08]. In both measurements, the determination of the cyclotron frequency was based on the detection of image currents that the motion of the ion induced in detection circuits attached to trap electrodes [WD75]. Another measurement technique is the time-of-flight ion cyclotron resonance (TOF-ICR) technique [GKT80]. With this method, Solders et al. determined the proton mass with an uncertainty of $1.8{\cdot}10^{-10}$ [SBN+08]. Common to all of these measurements is the precise knowledge of the mass of the reference ion, ideally ^{12}C since the atomic mass unit is defined as 1 u$=m(^{12}\mathrm{C})/12$, in order to get a measure for B.

The most precise mass measurements were all carried out with singly charged or low charged ions of light elements. But there are applications, that require mass measurements of heavier elements with comparable uncertainties. One of these applications is, e.g., the precise determination of the Q-value of the β^--decay

$$^{187}\mathrm{Re} \rightarrow {}^{187}\mathrm{Os} + \bar{\nu}_e + e^-$$

from the measurement of the mass-ratio between ^{187}Re and ^{187}Os. This measurement needs to be done for the following reason: Due to the extremely small $Q = (m(^{187}\mathrm{Re}) - m(^{187}\mathrm{Os}))c^2 \approx 2.47$ keV [GFGV00], the endpoint of the β-spectrum of the mentioned decay is very sensitive to the mass $m_{\bar{\nu}}$ of the electron anti-neutrino. The "microcalorimeter arrays for a rhenium experiment" (MARE) [NAC+10] is dedicated to the determination of $m_{\bar{\nu}}$ via the β-spectrum's endpoint with an uncertainty of 0.2

eV. As the MARE data will also yield a Q-value of the β-decay, a Q-value determined independently with a mass-ratio measurement can be used to check the MARE results for hidden systematic errors. Due to the smallness of Q, the mass-ratio needs to be determined with an uncertainty on the level of 10^{-10} to obtain a Q-value with the same uncertainty as MARE.

The PENTATRAP experiment, which is currently being built at the Max-Planck-Institut für Kernphysik, Heidelberg, is dedicated to the extension of the range of mass measurements with uncertainties on the order of 10^{-11} to the region of medium- and high-Z elements. In order to obtain cyclotron frequencies that are high enough for the precision that is aimed at, mass measurements will be carried out with highly charged ions, produced by so-called Electron Beam Ion Traps (EBITs) [CDMU99, DRE]. Although the ions will be created externally and the system thus needs to be open, excellent vacuum conditions with pressures smaller than 10^{-13} mbar will be provided in the trap region. Cyclotron frequencies will be determined by measuring the eigenfrequencies of an ion in a trap with the image current method [WD75]. The experiment will host five identical Penning traps. With two ions of different species stored in traps next to each other, this will allow for an exchange of the ion species in a trap within a few hundred milliseconds by adiabatically transporting the ions one trap further [RBC+11]. This will mimize measurement times and thus uncertainties due to magnetic and electric field drifts. Furthermore, one trap will be used for continuous monitoring of magnetic field fluctuations.

High-precision mass measurements in the PENTATRAP experiment have to be carried out with single ions in the traps. As the resulting image currents will be on the order of fA, highly sensitive detection electronics is required to convert these tiny currents into signals with high signal-to-noise ratio. As the axial frequency detection unit, i.e. the detection unit for the measurement of the motional frequency along the magnetic field lines, can be used both for the direct determination of the axial frequency as well as for the indirect determination of the other eigenfrequencies [CWB+89, VDS+04, SWSB11], it plays a crucial role in high-precision mass measurements. For a particularly high signal-to-noise ratio, this detection unit employs a resonator with a superconducting coil, that provides a very high impedance at resonance, for the conversion of the image currents to voltages. This signal is amplified by low-noise amplifiers and converted into the frequency range of an FFT analyzer with a down converter, that provides a high level of suppression of noise from frequency ranges other than the range of interest.

The detection electronics for PENTATRAP is the main topic of this thesis, which is organized as follows:

Chapter 2 provides a short introduction to Penning trap mass spectrometry as well as an overview of the PENTATRAP setup. Furthermore, a possible measurement scheme is presented.

In the beginning of Chapter 3, the detection of an ions' motional eigenfrequencies in a Penning trap via image currents will be discussed. Following, an overview of the Penning trap related electronics in the PENTATRAP experiment is given. Then,

detection electronics that was set up, tested and optimized within this thesis is treated in more detail, in particular the axial frequency down converter providing sideband suppression.

An amplifier based on a SQUID is an alternative to the cryogenic axial amplifier used in the PENTATRAP experiment. The main benefit of such an amplifier is negligible $1/f$ noise in the axial frequency range. To date, there is only one Penning trap experiment worldwide that has employed a SQUID for the detection of an ion's axial frequency [WLB+88]. First steps that were taken towards the integration of a SQUID based amplifier into the PENTATRAP setup are presented in Chapter 4. In the beginning of this chapter, basic principles underlying a SQUID are introduced. In the second part of the chapter, results of first experimental steps with a SQUID are presented.

The shielding of a SQUID in a strong magnetic field is subject of Chapter 5. The main part of this chapter is dedicated to an estimation of the influence of a magnetic shield on the homogeneity of the magnetic field in the PENTATRAP experiment.

The thesis will be concluded with a short summary and an outlook.

2. The PENTATRAP experiment

The high-precision Penning trap mass spectrometer PENTATRAP is currently being built at the Max-Planck-Institut für Kernphysik, Heidelberg. In Sec. 2.1, a short introduction to Penning trap mass spectrometry is provided. An overview of the PENTATRAP experiment is given in Sec. 2.2. Furthermore, a possible measurement scheme that uses the electronics developed within this thesis is presented in Sec. 2.3.

2.1. Penning trap mass spectrometry

Penning traps: In an ideal Penning trap, charged particles are trapped by a superposition of a strong homogeneous magnetic field and a weak quadrupolar electrostatic potential [Deh68,BG86]. The magnetic field $\vec{B}$ confines the particle in the radial plane, i.e. in the plane perpendicular to the direction of $\vec{B}$. Confinement in the axial plane is achieved by the quadrupolar potential $\Phi_e(\vec{r})$. Assuming that the magnetic field is directed in the z-direction, the quadrupolar potential is of the form

$$\Phi_e(\vec{r}) = A(\frac{1}{2}(x^2 + y^2) - z^2) = A(\frac{\rho^2}{2} - z^2), \tag{2.1}$$

where A determines the depth of the potential. A plot of the potential energy $\Phi(\vec{r})$ of the particle in the potential $\Phi_e(\vec{r})$ is shown in Fig. 2.1.

Since the equipotential lines are hyperbolae, as can be seen from Fig. 2.1, the quadrupolar potential can be obtained by applying voltages to electrodes, which are formed as hyperbolae of revolution [DW68]. This type of trap is called hyperbolical Penning trap. It is sketched in Fig. 2.2(a). Using the notation in this figure, the prefactor in Eq. (2.1) is given by $A = U_0/2d^2$, where U_0 is the voltage between the central ring electrode and the outer endcaps. $d \equiv ((\rho_0^2/2 - z_0^2)/2)^{-1/2}$ is the characteristic trap dimension. Alternatively, cylindrical electrodes can be used. Designed properly, this yields the same potential in the central volume of the trap [GHR89]. A cylindrical Penning trap is shown in Fig. 2.2(b).

Motion of an ion in a Penning trap: In the absence of the quadrupolar field, an ion in a homogeneous magnetic field $\vec{B_0}$ is subject to the Lorentz force. Therefore, it performs a circular motion in the radial plane at the free cyclotron frequency

$$\omega_c = \frac{qB_0}{m}, \tag{2.2}$$

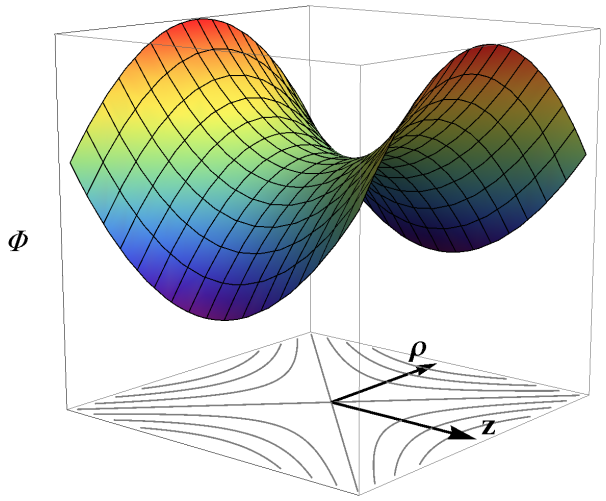

Figure 2.1.: Potential energy of a charged particle in a quadrupolar electrostatic potential. The sign of the electrostatic potential has been chosen such that the particle is confined in the z-direction. Equipotential lines are shown on the bottom of the plot.

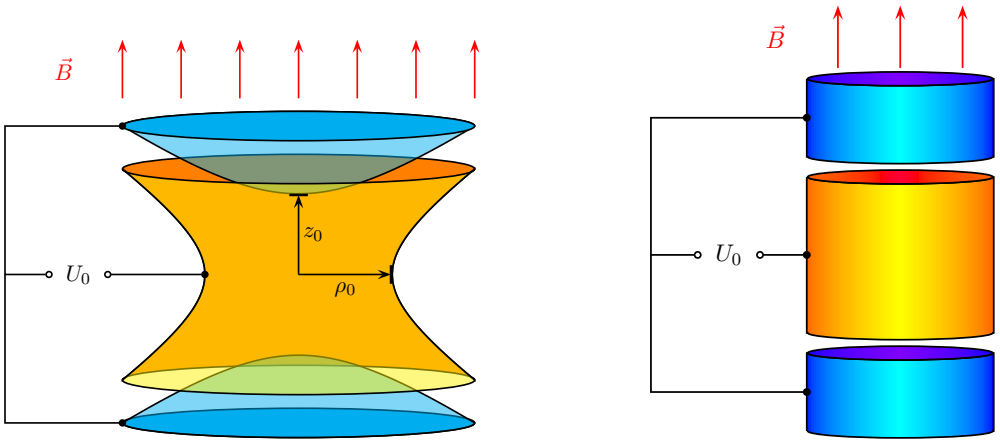

(a) Hyperbolical Penning trap

(b) Cylindrical Penning trap.

Figure 2.2.: Schematics of Penning traps with differently shaped electrodes are shown. Courtesy of Jochen Ketter.

where q/m is the charge-to-mass ratio of the ion.

In the presence of the quadrupolar potential, the motion of the ion is a superposition of three harmonic eigenmotions. In the axial direction, the ion oscillates in the harmonic potential with the angular frequency

$$\omega_z = \sqrt{\frac{qU_0}{md^2}}. \tag{2.3}$$

In the radial plane, the motion consists of two independent motions, the fast reduced cyclotron motion (ω_+) and the slow magnetron motion (ω_-) at the angular frequencies

$$\omega_\pm = \frac{\omega_c}{2} \pm \sqrt{\left(\frac{\omega_c}{2}\right)^2 - \frac{\omega_z^2}{2}}. \tag{2.4}$$

The resulting motion of the ion is sketched in Fig. 2.3. For typical magnetic fields and electrostatic potentials, the eigenfrequencies follow the hierachy

$$\omega_+ \gg \omega_z \gg \omega_-. \tag{2.5}$$

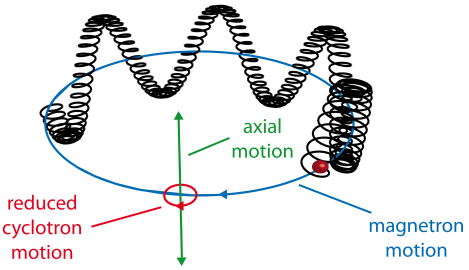

Figure 2.3.: Motion of an ion in a Penning trap. It is a superposition of three harmonic eigenmotions, called axial, magnetron and reduced cyclotron motion, respectively. For details see text.

Mass determination: For a given magnetic field strength B_0, the charge-to-mass ratio q/m can be directly deduced from the free cyclotron frequency $\omega_c = qB_0/m$. Although ω_c itself is not the frequency of an eigenmotion of the ion in a Penning trap, it can be obtained from the eigenfrequencies:

$$\omega_c = \sqrt{\omega_+^2 + \omega_-^2 + \omega_z^2}. \tag{2.6}$$

This relation, which is called the "invariance theorem", even holds for Penning traps with a misalignment between the magnetic field and the quadrupolar potential, as well as for traps with an elliptic electrostatic potential in the radial plane [BG82, Gab09]. Therefore, the mass of an ion can be determined by measuring its three eigenfrequencies in the trap.

2.2. PENTATRAP setup

An overview of the planned setup of the PENTATRAP experiment is shown in Fig. 2.4. Highly charged ions are produced by an Electron Beam Ion Trap (EBIT) [CDMU99, DRE]. A beamline containing several ion-optical elements is used for the transport of the ions from the EBIT to the trap region. The beamline contains two pulsed drift tubes to slow down the ions, so that they can be captured in the traps. A copper vacuum chamber hosts the trap stack, which consists of five Penning traps. A strong and homogeneous magnetic field for the Penning traps is provided by a superconducting 7-T magnet. The bore of the magnet is cooled by the same liquid helium reservoir as the magnets' coils. The trap chamber will be placed in this bore and therefore cooled down to 4 K. Eigenfrequencies of single ions in the traps will be detected non-destructively via image currents induced by the ions (see Sec. 3.1). The first stage of the detection system is placed in the cold bore of the magnet in a copper vacuum chamber directly beneath the trap chamber. Both the trap chamber and the electronics chamber are kept at a vacuum of better than 10^{-13} mbar. At the top flange of the magnet, small copper boxes hosting room temperature electronics are situated.

Details on the ion sources, the magnet and the traps will be provided in the following paragraphs. More extensive treatments of these topics can be found in [RBC+11] and [RBD+11]. An overview of the electronics involved in the experiments will be presented in Sec. 3.2.

Ion sources: For the commissioning of PENTATRAP and first experiments, the commercial room temperature Electron Beam Ion Trap Dresden EBIT3 (from DREEBIT GmbH) will provide access to highly charged ions. With a maximum electron energy of 15 keV, the EBIT is capable of complete ionization for atomic numbers $Z \leq 30$ [DRE]. For medium Z, up to He-like ions and for high Z, up to Ne-like ions can be produced. For heavier highly charged ions, the experiment will be connected to the Heidelberg EBIT [CDMU99]. Electron beams with energies up to 100 keV and currents of more than 500 mA are compressed by the field of a superconducting magnet in this EBIT [CBB+04]. Production of, e.g., He-like mercury has been achieved [GCB+05].

Magnet: The magnet is a 7-T superconducting magnet with a vertical cold bore of 160 mm diameter. In its central region, the magnet provides a very homogeneous field over a range of 12 cm. The exact field distribution in this region as well as the influence of magnetic field inhomogeneities on the achievable precision in mass measurements will be addressed in Sec. 5.2. The gas pressure and the helium level in the liquid helium reservoir of the magnet will be stabilized to improve the temporal stability of the magnetic field. Furthermore, drifts of vertical stray fields will be sensed with a flux-gate magnetometer and compensated with a pair of Helmholtz coils placed outside of the magnet. With these measures, a temporal stability on the order of 10^{-11}/h is aimed at [RBC+11].

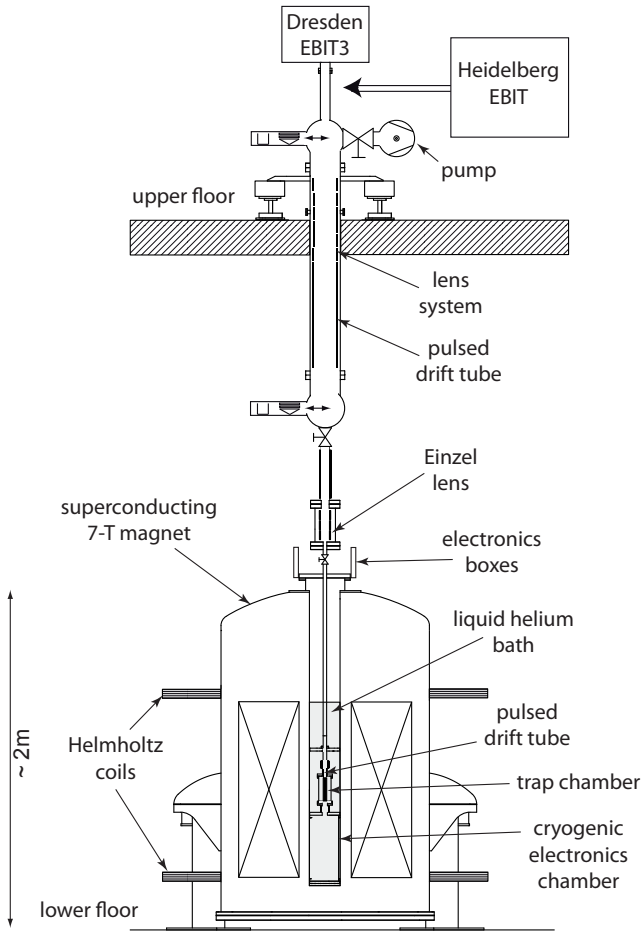

Figure 2.4.: Setup of the PENTATRAP experiment. The setup is distributed over two floors. Highly charged ions are produced either by a small room temperature EBIT [DRE] or the Heidelberg EBIT [CDMU99]. A beamline provides connection from the EBITs to the trap region. The traps are placed in the cold bore of a superconducting 7-T magnet. The cyrogenic detection electronics is placed in a copper chamber beneath the trap chamber. Two of the boxes at the top flange of the magnet hosting room temperature electronics are shown. For details see text. Courtesy of Julia Repp.

Traps: The trap stack consists of five identical cylindrical Penning traps. A drawing of the traps can be found in Fig. 2.5. Due to the cylindrical geometry of the traps, ions can be easily exchanged between the traps. The traps were designed to be compensated

and orthogonal [GHR89]. As the highly homogeneous region of the magnet is ∼12 cm long, the length of a single trap is 24 mm. The inner radius was chosen to be 5 mm, which keeps both the influence of image charge effects and the interaction between ions in adjacent traps on an acceptable level [RBD+11]. Trap electrodes are made of OFHC copper and the spacers between the electrodes are made from sapphire. The electrodes are furthermore gold plated to minimize patch potentials on the surfaces [RBC+11].

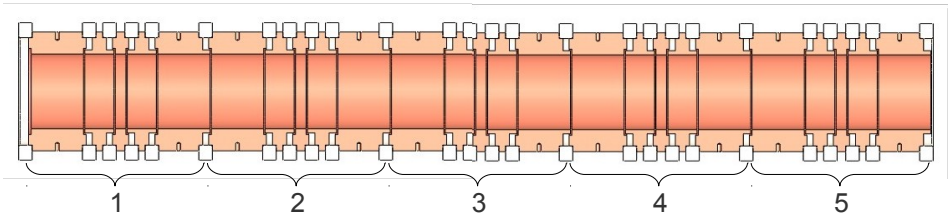

Figure 2.5.: Drawing of the trap stack. The stack consists of five identical cylindrical Penning traps. For details see text.

2.3. Mass and mass-ratio measurements

Both in mass and mass-ratio measurements, the cyclotron frequencies of two different ion species have to be measured. In mass measurements, the second species is used as magnetic field gauge and has to be of well-known mass.

In the PENTATRAP experiment, eigenfrequencies of ions in the five traps can be measured simultaneously. In the following, a mass-ratio measurement scheme taking advantage of the five trap setup and the simultaneous frequency determination is presented [RBC+11]: At a certain time t_1 three ions of two different species with charge-to-mass ratios q_1/m_1 and q_2/m_2 are loaded into the three inner traps (2, 3, 4) as shown in Fig. 2.6. The synchronous measurement of the eigenfrequencies of the ions in trap 3 and 4 yields the cyclotron frequency ratio

$$R_1 = \frac{\omega_c(z_3,t_1)}{\omega_c(z_4,t_1)} = \frac{q_2 B(z_3,t_1)/m_2}{q_1 B(z_4,t_1)/m_1} = \frac{m_1}{m_2}\frac{q_2}{q_1}\frac{B(z_3,t_1)}{B(z_4,t_1)}, \tag{2.7}$$

where, e.g., $B(z_3,t_1)$ is the axial magnetic field seen by the ion averaged over its axial amplitude and the measurement time. After the determination of R_1, all three ions are moved adiabatically one trap further to their right. This exchanges the ion species between trap 3 and 4, as can be seen in Fig. 2.6. The measurement of the eigenfrequencies in this configuration at time t_2 gives the cyclotron frequency ratio

$$R_2 = \frac{\omega_c(z_3,t_2)}{\omega_c(z_4,t_2)} = \frac{q_1 B(z_3,t_2)/m_1}{q_2 B(z_4,t_2)/m_2} = \frac{m_2}{m_1}\frac{q_1}{q_2}\frac{B(z_3,t_2)}{B(z_4,t_2)}. \tag{2.8}$$

Under the assumptions that the field configuration has not changed inbetween the measurements and that the ions experience the same axial field averaged over their axial amplitudes, the mass-ratio between the ions of species 1 and 2 is given as

$$\frac{m_1}{m_2} = \frac{q_1}{q_2}\sqrt{\frac{R_1}{R_2}}. \tag{2.9}$$

After this measurement cycle, the ions can be shifted back into their initial position and the measurement can start again.

The easy exchange of ions in the traps will allow for fast measurement cycles. This will reduce the influence of temporal drifts of both the magnetic field and the trap potentials. Furthermore, trap 1 (in Fig. 2.6), which has not been used in the scheme described above, can be used to monitor the magnetic field by continuously measuring the cyclotron frequency of a reference ion, e.g. $^4He^{2+}$. Under the assumption that drifts of the magnetic field are global, this data can be used to correct for magnetic field drifts.

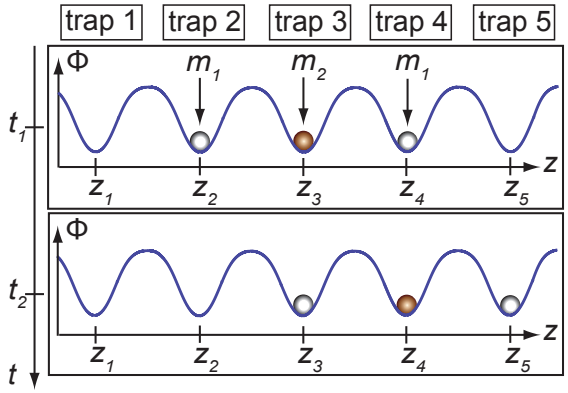

Figure 2.6.: Proposed mass-ratio measurement scheme for the PENTATRAP experiment [RBC+11]. Three ions of two different species, indicated by red and white spheres, are situated in the traps 2 - 4. The traps are depicted by their electrostatic potential in the axial direction. After a simultaneous measurement of the cyclotron frequencies of the ions in trap 3 and 4, each ion is adiabatically shifted to the trap to its right. Then another simultaneous measurement of the cyclotron frequencies of the ions in trap 3 and 4 is performed. From these measurements, the mass-ratio m_1/m_2 can be determined. For further details see text.

3. Detection

3.1. Detection principle

The measurement of the eigenfrequencies of an ion in a Penning trap of the PENTATRAP experiment is based on the detection of image currents that the ion induces in a circuit consisting of two trap electrodes connected by an impedance.

To illustrate the principle, an ion of charge q oscillating between two parallel conducting plates is considered. The plates are connected by an impedance $Z(\omega)$, as shown in Fig. 3.1. The motion of the ion perpendicular to the plates causes a temporal change of the image charges induced on the plates. Therefore, a current, which is called the image current, flows between the plates. For an ion oscillation $z(t) = z_0 \sin(\omega_0 t)$ perpendicular to two infinitely extended parallel plates separated by a distance d, the image current I and the voltage U_{ind} across the impedance are given by [Sho38]:

$$\begin{aligned} I(t) &= \frac{q \cdot \dot{z}}{d} = q\omega_0 \frac{z_0}{d} \cos(\omega_0 t), \\ U_{\text{ind}}(t) &= Z(\omega_0) q\omega_0 \frac{z_0}{d} \cos(\omega_0 t). \end{aligned} \tag{3.1}$$

This relation is not limited to infinite parallel plates, but can be applied to Penning traps as well [WD75].

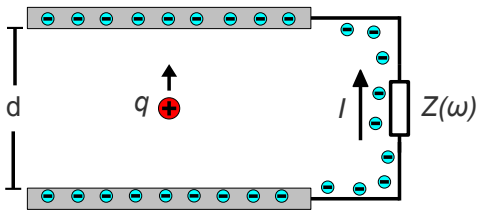

Figure 3.1.: An ion of charge q is moving perpendicular to two parallel conducting plates. The two plates are connected by an impedance $Z(\omega)$. A current of electrons, representing charge carriers in general, is present due to the temporal change of the image charges that are induced by the ion on the plate.

From Eq. (3.1) it can be seen that the voltage U_{ind} across the impedance Z is

oscillating at the same frequency as the ion. This is the basis for the non-destructive measurement of the eigenfrequencies of an ion in a Penning trap.

The image currents of single ions are usually very small. For a $^{12}C^{3+}$ ion, e.g., with an axial amplitude of 10 µm and an axial frequency of 600 kHz in a Penning trap with D_{eff} on the order of 1 mm, the axial image current has a peak amplitude on the order of ∼10 fA.

As the initial signal magnitude is proportional to the impedance, Z should be as large as possible for a high signal-to-noise ratio (SNR). A high-ohmic resistor cannot be used as impedance, as it would be bypassed by the trap capacitances, which are usually a few pF [Sta98]. Instead, parallel LCR tank circuits, consisting of the trap capacitances and an inductor of high quality factor Q, are commonly used. In Fig. 3.2 both the absolute value and the phase of the complex impedance of a tank circuit are displayed near the resonance frequency $\omega_{LC} = (LC)^{-1/2}$. From Fig. 3.2(b) it can be seen that at ω_{LC}, the reactance of the inductor compensates the reactance of the total capacitance. Furthermore, the impedance is of maximum magnitude R at resonance. If the oscillation frequency of the ion is at ω_{LC}, the image current I leads to a voltage of $R \cdot I$ over the tank circuit.

A characteristic quantity of the tank circuit is the quality factor Q, which is related to the height R and the width $\Delta\omega$ (see Fig. 3.2(a)) of the resonance curve as follows [Ros83]:

$$Q = \frac{R}{\omega_{LC} L} = R\omega_{LC} C = \frac{\omega_{LC}}{\Delta\omega}. \tag{3.2}$$

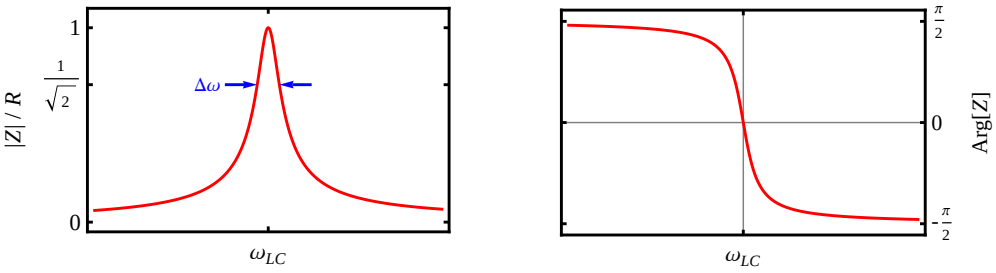

(a) Absolute value of the impedance. $\Delta\omega$ denotes the full width at $R/\sqrt{2}$, where R is the impedance at the resonance frequency ω_{LC}.

(b) Phase of the complex impedance. The phase is zero at ω_{LC}. Therefore, the impedance is purely real at resonance.

Figure 3.2.: Impedance of a parallel LCR circuit with a resonance frequency of $\omega_{LC} = (LC)^{-1/2}$.

For the spectrum of the signal across the tank circuit, two situations can be distin-

guished: Either the detected eigenmotion is or is not in thermal equilibrium with the tank circuit.

The excess energy of an eigenmotion which is not in thermal equilibrium with the tank circuit will be dissipated in the circuit's resistance. This results in a voltage across the tank circuit. Therefore, the spectrum of the signal measured across the impedance yields the noise spectrum of the impedance superimposed with a peak at the eigenfrequency of the ion. Maximum peak amplitudes can be obtained, when the eigenfrequency of the ion matches the resonance frequency of the tank circuit. Due to the dissipation, the kinetic energy of the ion is successively reduced. This can be used for resistive cooling [BH08].

When the ion is in thermal equilibrium with the tank circuit, the ion in the trap can be described as a series LC circuit with a very high quality factor and a resonance frequency equal to the eigenfrequency of the ion [WD75]. As the impedance of a series LC circuit is zero at resonance, the ion shunts the tank circuit. If the eigenfrequency of the ion coincides with the resonance frequency of the tank circuit, a dip in the middle of the noise spectrum of the tank circuit can be observed.

3.2. Electronics overview

This section will provide an overview of the Penning trap related electronics in the PENTATRAP experiment. This electronics can be divided in three categories: First the electronics that is needed to apply the trap voltages to the trap electrodes, second the electronics that is needed to excite ions in the traps and third the detection electronics.

Trap voltages: For the commissioning of the PENTATRAP apparatus and first experiments, the trap voltages will be delivered by the commercial high-precision voltage source UM 1-14 from Stahl electronics [Sta]. The output voltage of this source ranges down to -14 V and is specified to have a temporal stability of typically ± 0.8 ppm per day [Sta08]. In order to remove HF noise, the voltages will be filtered by RC low-pass filters at the top of the magnet, before they are guided into the cryogenic region of the experiment. Before the voltages are applied to the trap, they will be filtered by a second low-pass filter. This setup is drawn schematically in Fig. 3.3.

Exciation signals: The signals for the dipolar and quadrupolar excitation of ions in the various traps will be provided by Agilent 33250A signal generators. These excitations are needed to increase motional amplitudes and to couple eigenmotions, respectively. In order to reduce the influence of external noise on the exciation SNR, the inital excitation amplitude will be chosen higher than needed and then reduced by two capacitive voltage dividers. One of the dividers is placed on top of the magnet and one in the cryogenic region in adjacency to the traps. A schematic of the exciation electronics for an axial excitation is shown in Fig. 3.4. In Fig. 3.5 a preliminary

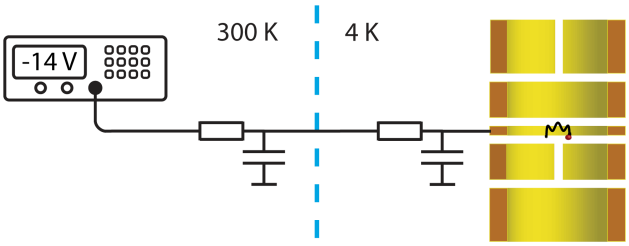

Figure 3.3.: The electronics involved in the trap voltage supply is shown exemplarily for a ring electrode. The voltage, provided by an UM 1-14 voltage source, will be filtered at the top of the magnet in the room temperature region and a second time before the application to the electrode.

schematic overview of the excitation signals applied to the different electrodes can be seen. In this configuration, axial excitation signals will be applied to one of the endcaps in each trap. Radial dipolar and quadrupolar excitation signals will be applied to one half of the other endcap, which is splitted in halves. Other configurations, e.g. with splitted correction electrodes for higher quadrupolar coupling strengths, are under discussion.

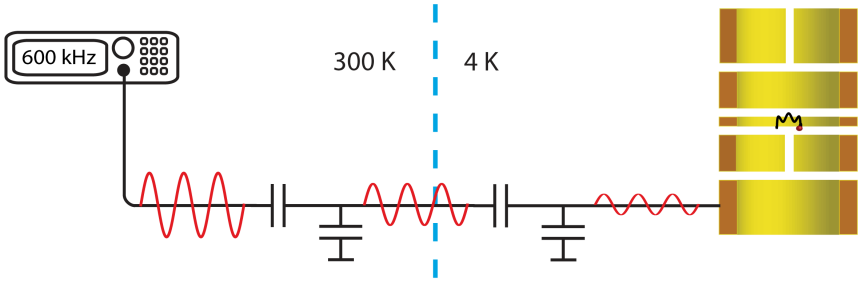

Figure 3.4.: The electronics involved in the exciation of the axial mode is shown. The excitation signal will be provided by an Agilent 33250A signal generator. To reduce the influence of external noise on the excitation SNR, the initial signal amplitude will be chosen higher then needed and then damped by two capacitive voltage dividers in sequence. The sinusoidal signals indicate the exciation signal amplitude after each component.

Detection electronics: Besides the exciation signals, Fig. 3.5 shows a preliminary configuration of the detection units connected to the electrodes of the five Penning traps. For the detection of the axial frequency, the image current induced by the axial motion will be picked up at a correction electrode. The other correction electrode will be splitted, and the image current induced by the reduced cyclotron motion will be

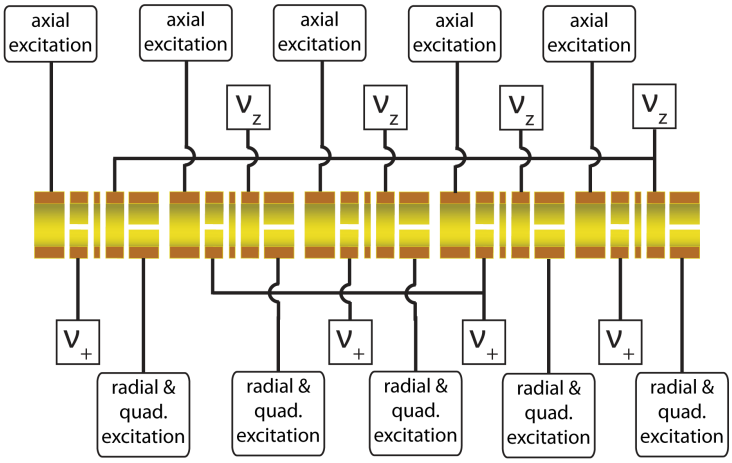

Figure 3.5.: Preliminary schematic overview of the exciation signals and the detection units connected to the electrodes of the five Penning traps in the PENTATRAP experiment. The detection units are labeled by the frequency that should be detected with them. For detection and exciation, some electrodes will be split into halves. Other configurations are under discussion.

picked up at one of the halves. Other configurations are under discussion: If, e.g., both corrections electrodes of each trap were splitted, the axial signal would have to be picked up at an endcap.

Due to the invariance theorem (see Eq. (2.6)) and the hierarchy of the eigenfrequencies (see Eq. (2.5)), the relative uncertainty of the magnetron frequency influences the precision of the cyclotron frequency determination much less than the relative uncertainties of the other eigenfrequencies. Therefore, a direct measurement of the magnetron frequency will not be performed.

Exemplarily, a schematic of an axial detection unit is shown in Fig. 3.6. The image current induced by the axial motion is picked up at a correction electrode and converted into a voltage by the tank circuit, which contains an inductance with a high quality factor. The signal is amplified by two amplifiers, one in the cryogenic region and one in the room temperature region. After the down conversion to lower frequencies, the signal can be detected with an FFT analyzer. The single components of the axial and the cyclotron detection units of the PENTATRAP experiment will be presented in the following two sections.

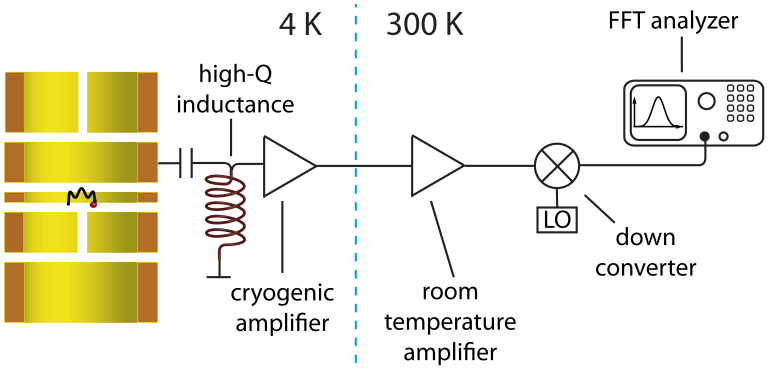

Figure 3.6.: Schematic of an axial detection unit. The image current induced by the axial motion is picked up at one of the correction electrodes and converted into a voltage by a resonant tank circuit. The resulting signal is amplified by a cryogenic amplifier before it is guided to the room temperature region. There it is amplified again, converted to lower frequencies and detected by an FFT analyzer. The box labeled LO indicates the local oscillator of the down converter.

3.2.1. Cryogenic detection electronics

In order to keep the thermal noise of the detection electronics as low as possible, the first stage of the detection unit is placed in the cryogenic region of the experiment near the traps.

The most important detection units are the axial detection units: Not only can they be used for the detection of the axial frequency, but also for detection of the cyclotron frequency with various indirect detection techniques [CWB+89, VDS+04, SWSB11]. The axial resonators, which serve as high-Q inductances in the axial tank circuits, are toroidal shaped superconducting NbTi coils placed in a OFHC copper housing. The coil is shown in Fig. 3.7(a). Properties of a prototype can be found in Tab. 3.1. The cryogenic axial amplifiers are based on GaAs field-effect transistors (FETs), which are operable at 4 K, whereas Si based devices suffer from “carrier freeze-out" at temperatures below 30 K [KL93]. Properties of the axial amplifiers can be found in Tab. 3.2.

The cyclotron resonators consist of helical high-purity copper coils placed in OFHC copper housings. A cylotron resonator can be seen in Fig. 3.7(b). The properties of a prototype can be found in Tab. 3.1. The cyclotron resonators serve for two purposes: First of all, they can be used for the direct detection of the image currents induced by the reduced cyclotron motion. Secondly, resistive cooling of the cyclotron motion is required, when the axial and the magnetron motion should be cooled below the temperature of the environment using the sideband cooling technique [BG86]. The cryogenic cyclotron amplifiers are based on GaAs FETs. Properties of the cyclotron

amplifier can be found in Tab. 3.2.

As mentioned above, the reduced cyclotron frequency can be measured indirectly. Such measurements require that the reduced cyclotron motion can be decoupled from the cyclotron tank circuit. This can be realized with Q-switches that damp the resonance of the tank circuit. A first implementation of a Q-switch will be subject of Sec. 3.3.

(a) Axial toroidal coil. The coil is made from 75 µm thick NbTi wire wound on a teflon torus. The torus is wrapped with teflon tape. The two copper wires soldered to the ends of the coil can be seen.

(b) Helical cyclotron coil in open housing. The coil is made from high-purity copper wire wound on a hollow teflon cylinder. The housing is made from OFHC copper. It is polished on the inside.

Figure 3.7.: Components of the axial and the cyclotron detection tank circuits [Rou11a].

Resonator	Q	L / µH	C / pF
axial	∼65000	∼3400	∼10
cyclotron	∼4000	∼2	∼3.5

Table 3.1.: Quality factors, inductances and self-capacitances of the resonator prototypes are presented.

Amplifier	Gain / dB	Voltage-noise density / (nV/$\sqrt{\text{Hz}}$)
axial	>10	∼0.8 at 600 kHz
cyclotron	>8	∼0.3 at 27 MHz

Table 3.2.: Gain and voltage-noise density of the cryogenic amplifiers.

3.2.2. Room temperature detection electronics

As can be seen from Fig. 3.6, the output signal of the cryogenic amplifier is amplified another time before it is converted to lower frequencies and analyzed by an FFT analyzer. In the axial detection setup, both amplification and down conversion will be performed by a single device, which will be subject of Sec. 3.4.2. The reduced cyclotron signal will be amplified with Mini-Circuits ZFL-500LN amplifiers and converted to lower frequencies with Mini-Circuits ZAD6+ mixers.

3.3. Q-switches

A Q-switch can be build with a simple switch, which connects a capacitor in parallel to the cyclotron tank circuit in order to shift and damp the resonance of the circuit when the ion needs to be decoupled from the tank circuit. A first Q-switch was build on the basis of an SKY13316-12LF GaAs switch, which was specified to have an isolation of more than 80 dB between RF in- and output for frequencies below 60 MHz at room temperature [Sky08]. The test setup for the Q-switch is shown in Fig. 3.8. The Q-switch and the cyclotron resonator were placed in a cryostat and cooled down by a cryocooler. The switch state was set with two control voltages. The resonance of the tank circuit was recorded with a network analyzer. In- and output of the network analyzer were weakly capacitively coupled to the tank circuit.

Results of the test measurements are presented in Fig. 3.9. The blue resonance with the center frequency at 46.86 MHz shows the resonance for the closed switch, the red resonance with the center frequency at 52.62 MHz shows the resonance for the open switch. The resonances yielded quality factors of Q=1388±19 for the closed switch and Q=111.5±2.7 for the open switch. The resonance for the open switch is considerably shifted and damped compared to the resonance of the free resonator with a resonance frequency of ∼60 MHz and a Q of 4000. Shift and damping of the resonance suggest to describe the open switch as a ∼1.8 pF capacitor with a very poor quality factor and not as an isolator. Therefore, the switch cannot be operated in the originally intended scheme, as the switch would heavily damp the tank circuit. An alternative scheme would be to have the switch closed for regular operation of the tank circuit and to open the switch to damp the circuit. But in this scheme, the intrisic quality factor of the coupling capacitor would limit the Q of the tank circuit. It can be concluded that the SKY13316-12LF switch is not suitable to build a Q-switch. A number of other

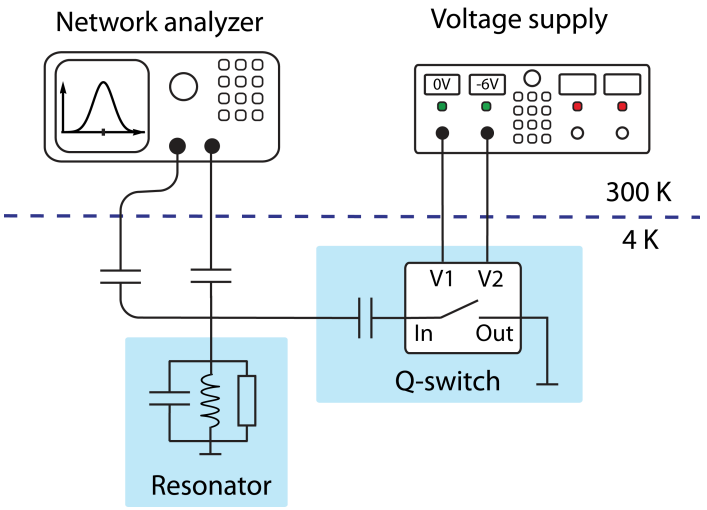

Figure 3.8.: Test setup for the Q-switch based on an SKY13316-12LF GaAs switch. Cyclotron resonator and Q-switch were placed in a cryostat and cooled by a cryocooler. The resonator is represented by the LCR circuit it forms intrisically. The Q-switch could switch 2.2 pF in parallel to the tank circuit. The switch state was controlled by the two voltages V1 and V2. Resonances were recorded with a HP 4195A network analyzer that was weakly capacitively coupled to the tank circuit.

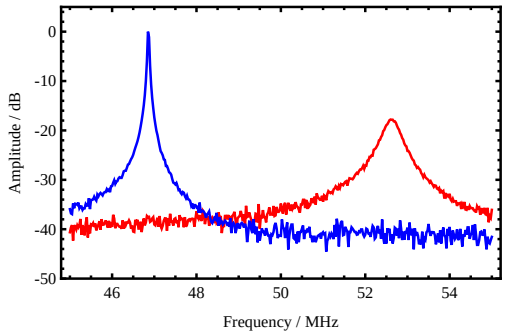

Figure 3.9.: Resonances of the cyclotron resonator with the Q-switch opened (red curve) and the Q-switch closed (blue curve). The resonances were recorded with a network analyzer. Amplitudes are given relative to the peak amplitude of the resonance with the Q-switch closed.

GaAs switches will be tested soon in order to find a more suitable device.

3.4. Axial frequency down converters

3.4.1. Theoretical considerations

Fast Fourier transform (FFT) analyzers are commonly used to measure spectra of signals when both a high frequency resolution and a high dynamic range are required. The upper frequency limit of such analyzers, or more generally of any device that relies on the measurement of signals in the time domain, is determined by the maximum sampling rate of the analog-to-digital converter (ADC) used [Pat09]. For example, the maximum frequency of an Agilent 35670A one channel FFT analyzer is 102.4 kHz [Agi09]. Signals containing frequencies higher than the maximum frequency have to be converted down into the frequency range of the analyzer to be detectable. This section will provide the theoretical background of a down converter, which has very good noise properties in a sense that it rejects the down conversion of noise from frequency ranges other than the range of interest around the signal.

A down converter shifts the frequency ν_{in} of a sinusoidal signal to the so-called intermediate frequency $IF = \nu_{in} - \nu_{LO}$ by multiplying the signal with a sinusoidal local oscillator (LO) signal of frequency ν_{LO}:

$$\begin{aligned} U_{out}(t) &\propto \sin(2\pi \cdot \nu_{in} t) \cdot \sin(2\pi \cdot \nu_{LO} t) \\ &= \frac{1}{2}(\sin(2\pi \cdot (\nu_{in} - \nu_{LO})t) + \sin(2\pi \cdot (\nu_{in} + \nu_{LO})t). \end{aligned} \tag{3.3}$$

For down conversion, the signal at the sum frequency has to be removed by a filter. Since any signal can be decomposed into a finite or infinite number of sine and cosine functions, the whole spectrum of a signal can be shifted by multiplication with an LO signal.

Common circuits in electronics for the multiplication of signals are, e.g., ring modulators and Gilbert cells [TS02]. In both circuits, one of the signals is used to periodically modulate the transmission of the other signal through certain elements. In ring modulators, these elements are diodes and in Gilbert cells, they are transistors.

3.4.1.1. Single sideband down conversion

When a signal is converted down, the local oscillator is adjusted such that the complete frequency range of interest is either in the upper sideband, i.e. above the local oscillator frequency ν_{LO}, or in the lower sideband, i.e. below ν_{LO}. A simple multiplier followed by a low-pass filter converts both signals from the upper and the lower sideband down into the same frequency range. That means, signals at frequencies $\nu_{LO} + IF$ and $\nu_{LO} - IF$ are converted to the same intermediate frequency IF and get superimposed:

$$\begin{aligned} &(A_1 \sin(2\pi \cdot (\nu_{LO} + IF)t) + A_2 \sin(2\pi \cdot (\nu_{LO} - IF)t)) \cdot \sin(2\pi \nu_{LO} t) \\ \rightarrow &A_1 \sin(2\pi \cdot IF \cdot t) + A_2 \sin(-2\pi \cdot IF \cdot t) = (A_1 - A_2) \sin(2\pi \cdot IF \cdot t). \end{aligned} \tag{3.4}$$

That means noise is added to the signal from the frequency range of interest and the SNR is reduced. Therefore, the unwanted sideband has to be rejected.

A so-called single sideband down converter is shown schematicly in Fig. 3.10. The main principle behind this setup is that the two mixers and the two phase shifters create two signals at IF, which are constructively superimposed for input signals from one sideband and destructively for the other sideband.

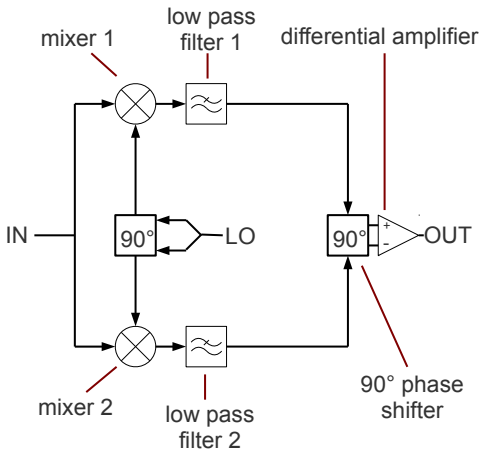

Figure 3.10.: Schematic of a down converter providing sideband rejection. Two signals at IF are created and their phase difference is manipulated in a way that the differential amplifier superimposes signals from one sideband constructively and signals from the other sideband destructively. For details see text.

To point out the interplay of the components shown in Fig. 3.10, the following example, for which calculations can be found in Tab. 3.3, is considered: A sinusoidal signal at frequency $\nu_{LO} + IF$ should be converted to an intermediate frequency IF. ν_{LO} is the local oscillator frequency that has been chosen such that the signal of interest is in the upper sideband. A sinusoidal signal from the lower sideband at frequency $\nu_{LO} - IF$ should be rejected in order not to disturb a measurement of the signal from the upper sideband.

At first, the signal from the upper sideband is considered. The signal is applied to the two mixers in the setup. The two local oscillator signals of the mixers are of equal frequency ν_{LO} and equal amplitude, but the LO signal for mixer 1 is 90° ahead in phase. The two signals after the low-pass filters behind the mixers are both at frequency IF and of equal amplitude, but the signal behind mixer 2 is 90° ahead in phase, as can be concluded from trigonometric identities. The second phase shifter increases the phase difference between the signal behind mixer 2 and the signal behind mixer 1 by another 90°, so that the signal behind mixer 2 is 180° ahead in phase. The differential amplifier therefore superimposes the two signals constructively.

Next, the signal from the lower sideband is considered. The signal is again applied

to both mixers and the properties of the two local oscillator signals are the same as in the case of the upper sideband. The two signals after the low-pass filters behind the mixers are both at frequency IF and of equal amplitude, but in this case, the signal behind mixer 1 is 90° ahead in phase. Therefore, the second phase shifter changes the phase difference between the signal behind mixer 2 and the signal behind mixer 1 to 0°. This results in a destructive superposition of the two signals by the differential amplifier (see Tab. 3.3).

	Upper sideband	Lower sideband
Input signal	$\sin((\omega_{LO}+\omega_{IF})t)$	$\sin((\omega_{LO}-\omega_{IF})t)$
After low-pass filter	$\frac{1}{2}\sin(\omega_{IF}t)$, $\frac{1}{2}\cos(\omega_{IF}t)$	$\frac{1}{2}\sin(-\omega_{IF}t) = -\frac{1}{2}\sin(\omega_{IF}t)$, $\frac{1}{2}\cos(-\omega_{IF}t) = \frac{1}{2}\cos(\omega_{IF}t)$
After 90° shifter	$\frac{1}{2}\sin(\omega_{IF}t)$, $-\frac{1}{2}\sin(\omega_{IF}t)$	$-\frac{1}{2}\sin(\omega_{IF}t)$, $-\frac{1}{2}\sin(\omega_{IF}t)$
After diff. amp.	$\sin(\omega_{IF}t)$	0

Table 3.3.: Examplary calculation for sinusoidal input signals from the upper and the lower sideband to the single sideband downconverter. Only time dependent parts of the signals are given. ω_{IF} and ω_{LO} are the angular frequencies corresponding to IF and ν_{LO}. If two signal functions are given in one cell, the upper one is associated with mixer 1 in Fig. 3.10 and the other one with mixer 2. The LO signal was given by $\cos(\omega_{LO}t)$ for mixer 1 and by $\sin(\omega_{LO}t)$ for mixer 2 in this calculation.

3.4.1.2. Passive polyphase filters

Key components in the down converter are the two phase shifters, which have to increase the phase difference between two incident signals by 90° while maintaining the equality of the amplitudes over the whole input and intermediate frequency range in which the down converter should provide sideband rejection. They can be realized with passive polyphase filters (PPFs), which show nearly ideal behaviour if designed properly.

A PPF is usually made up of multiple stages. Each stage consists of four identical resistors and four identical capacitors, as shown in Fig. 3.11.

Ideal passive polyphase filters: The voltage differences $\Delta I_{out,n} \equiv I_{out+,n} - I_{out-,n}$ (see Fig. 3.11) and $\Delta Q_{out,n}$ at the output of the n-th stage of an ideal multiple stage PPF are related to the voltage differences $\Delta I_{in,n}$ and $\Delta Q_{in,n}$ at the input as follows

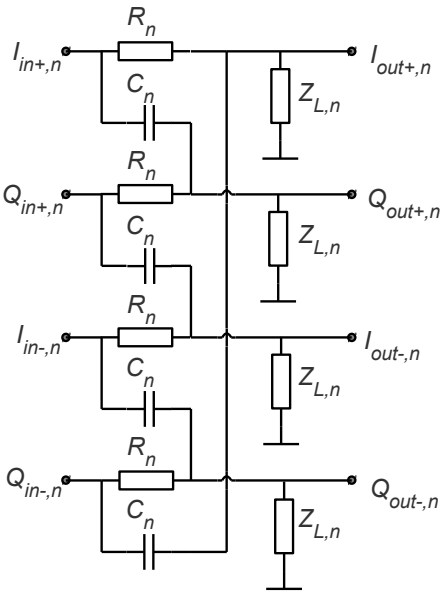

Figure 3.11.: n-th stage of a multiple stage passive polyphase filter, including the load impedances $Z_{L,n}$ [KSRH08]. Naming of the in- and output voltages is in accordance with the cited article.

[KSRH08]:

$$\begin{bmatrix} \Delta I_{out,n} \\ \Delta Q_{out,n} \end{bmatrix} = \frac{Z_{L,n}}{R_n + Z_{L,n} + i\omega C_n R_n Z_{L,n}} \begin{bmatrix} 1 & -i\omega C_n R_n \\ i\omega C_n R_n & 1 \end{bmatrix} \begin{bmatrix} \Delta I_{in,n} \\ \Delta Q_{in,n} \end{bmatrix}. \quad (3.5)$$

R_n and C_n are the component values of the resistors and capacitors, respectively, and $Z_{L,n}$ is the load impedance of the stage.

When the input is applied to the first stage of the PPF in a dual-feed manner as shown in Fig. 3.12, the following relation can be deduced from Eq. (3.5) [KSRH08]:

$$\frac{\Delta I_{out,1}}{\Delta Q_{out,1}} = \frac{1 - i\omega R_1 C_1}{1 + i\omega R_1 C_1}. \quad (3.6)$$

The absolute value A_{IQ} of this ratio is unity for all frequencies, independent of the values of R_1 and C_1, whereas the phase difference $\Delta\theta_{IQ}$ between the outputs is exactly 90° only at the pole frequency $\nu_1 = (2\pi R_1 C_1)^{-1}$. In Fig. 3.13(a), the steep red line shows the frequency dependence of $\Delta\theta_{IQ}$ of a one stage PPF with R=1.5 kΩ and

C=150 pF, corresponding to a pole frequency of $\nu \approx$707 kHz. It can be seen that less than 15 kHz away from the pole frequency, $\Delta\theta_{IQ}$ is 1° away from the ideal 90°. To improve the performance, one can use multiple stages with different pole frequencies distributed over the bandwidth in which the PPF is operated. The flat blue line in Fig. 3.13(a) shows $\Delta\theta_{IQ}$ at the output of a five stage PPF with R=1.5 kΩ for all stages and C_i=100, 150, 220, 330 and 470 pF, corresponding to pole frequencies of 226, 322, 482, 707 and 1061 kHz. A deviation of $\Delta\theta_{IQ}$ from 90° is hardly observable in the range of the figure. Fig. 3.13(b) shows $\Delta\theta_{IQ}$ over an extended frequency range for this five stage PPF, which, in fact, is the LO-PPF of a single sideband down converter that was build for PENTATRAP (see Sec. 3.4.2). It can be seen that the phase difference is exactly 90° only at the pole frequencies. But in the frequency range from the lowest to the highest pole frequency, the deviation from 90° is not more than 0.1°.

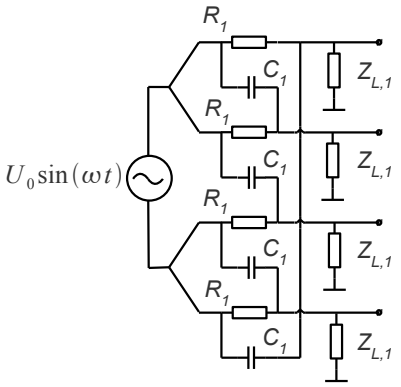

Figure 3.12.: Sinusoidal input signal at angular frequency ω applied to the first stage of a PPF in a dual-feed manner. This means, the upper two and the lower two input nodes are on the same potential.

This shows that a PPF consisting of multiple stages with proper pole frequencies [KSRH08] can be a good approximation of an ideal 90° phase shifter over a large frequency range. But it has to be pointed out that even an ideal PPF can never be an ideal 90° phase shifter over an extended frequency range. Therefore, it is more appropriate to state that a down converter as described in Sec. 3.4.1 using PPFs as phase shifters provides sideband suppression rather than sideband rejection. The level of sideband suppression that a PPF can provide, assuming that the rest of the down converter is working ideally, is given by the sideband suppression ratio [KSRH08]:

$$SSR(\omega) = \frac{1 + 2A_{IQ}(\omega)\cos(90° - \Delta\theta_{IQ}(\omega)) + A_{IQ}^2(\omega)}{1 - 2A_{IQ}(\omega)\cos(90° - \Delta\theta_{IQ}(\omega)) + A_{IQ}^2(\omega)}. \tag{3.7}$$

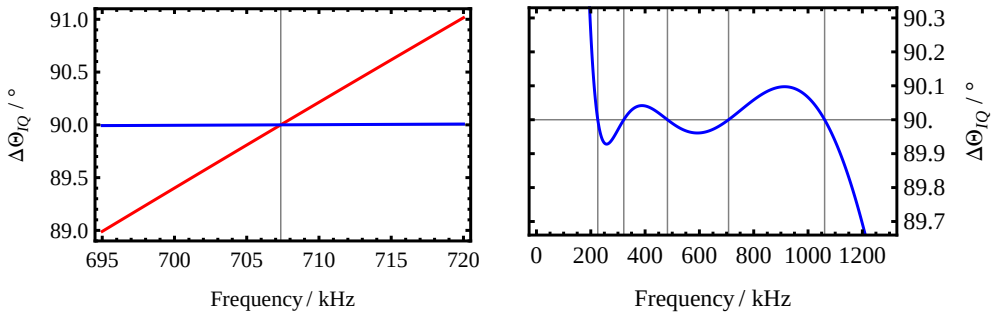

(a) Comparison of $\Delta\theta_{IQ}$ between a one stage PPF with a pole frequency of approximately 707 kHz (red line) and a five stage PPF with polefrequencies of approximately 226, 322, 482, 707 and 1061 kHz (blue line).

(b) $\Delta\theta_{IQ}$ for the five stage PPF over an extended frequency range. The vertical lines indicate the pole frequencies.

Figure 3.13.: Phase difference $\Delta\theta_{IQ}$ against input signal frequency for ideal PPFs with different numbers of stages. The input signal is assumed to be applied to the first stage in a dual-feed manner as shown in Fig. 3.12.

Real passive polyphase filters

Component value deviations: In a real PPF there are component value deviations among the resistors and the capacitors in each stage. This is shown in Fig. 3.14(a), where also deviations among the load impedances are included. If one calculates the potential at every node of the PPF seperately, one can see that deviations among the components and the load impedances destroy the symmetry that is underlying Eq. (3.5). The potential of the $Q_{out+,n}$ node in Fig. 3.14(a) for example is calulated by grounding all inputs but $Q_{in+,n}$, calculating the resulting potential at $Q_{out+,n}$ with voltage division rules, doing the same for the $I_{in+,n}$ input and superimposing both potentials [KSRH08]:

$$\begin{aligned} Q_{out+,n} &= \frac{(i\omega C_{n,1})^{-1} \parallel Z_{L,n,2}}{R_{n,2} + (i\omega C_{n,1})^{-1} \parallel Z_{L,n,2}} Q_{in+,n} + \frac{R_{n,2} \parallel Z_{L,n,2}}{(i\omega C_{n,1})^{-1} + R_{n,2} \parallel Z_{L,n,2}} I_{in+,n} \\ &= \frac{Z_{L,n,2}}{R_{n,2} + Z_{L,n,2} + i\omega R_{n,2} C_{n,1} Z_{L,n,2}} (Q_{in+,n} + i\omega R_{n,2} C_{n,1} I_{in+,n}), \end{aligned} \tag{3.8}$$

where ω is the angular frequency of the input signal. The pre-factors of the potentials in the second line of the equation have the same form as those appearing in Eq. (3.5). But since these factors are different from node to node due to the deviations, the expressions for the potentials at the four output nodes cannot be merged to an expression like Eq. (3.5).

In the case of an ideal PPF, it is not necessary to calculate the load impedances of a stage explicitly to obtain the phase difference $\Delta\theta_{IQ}$ and the amplitude ratio A_{IQ} between the I- and the Q-outputs of the final stage. This can be seen from Eq. (3.5), where $Z_{L,n}$ appears only in the pre-factor in front of the matrix. In the case of a real PPF, one has to calculate the potential at each node of the PPF explicitly to obtain $\Delta\theta_{IQ}$ and A_{IQ}. For each of these potentials, the load impedance at the corresponding node needs to be calculated. Due to deviations among the components of the PPF or the load impedances of the final stage, the load impedances within a stage can be different. Assuming that the n-th stage in Fig. 3.14(a) is not the final stage, the load impedance $\mathrm{Z}_{L,n,i}$ is given by [KSRH08]:

$$Z_{L,n,i} = (R_{n+1,i} + Z_{L,n+1,i} \parallel \frac{1}{i\omega C_{n+1,i-1}}) \parallel (\frac{1}{i\omega C_{n+1,i}} + Z_{L,n+1,i+1} \parallel R_{n+1,i+1}), \tag{3.9}$$

where the indices $i-1$, i and $i+1$ are modulo 4. With the load impedances of the final stage and the component values, one can calculate the load impedances of all stages recursively.

To analyze the influences of component value deviations, a model for the component value distributions was created. For different input frequencies ν, sets of PPFs were generated randomly according to this model. For each of these PPFs, $\Delta\theta_{IQ}$ and A_{IQ} were calculated. These quantities were then statistically analyzed.

In the model for the component value distribution it was assumed that the component value probability density for a set of components is a normal distribution. The center of the distribution is the nominal component value and the tolerance corresponds to an interval around the center with a half width of 3σ. Therefore, the model covers more than 99.7 % of the components. The probability density function for a set of 1.5 kΩ resistors with a tolerance of 1 % in this model is shown exemplarily in Fig. 3.14(b).

For the analysis of a PPF at a specific frequency, the nominal component values, the tolerances and the number of PPFs had to be specified. This number of PPFs was then randomly generated. For each of these PPFs, the load impedance and the potential at every node were calculated, using Eq. (3.8) and Eq. (3.9). From the potentials at the output nodes, $\Delta\theta_{IQ}$ and A_{IQ} were deduced. In the final step, mean value and standard deviation of $\Delta\theta_{IQ}$ and A_{IQ} of all PPFs were calculated. All these calculations were carried out with Wolfram Mathematica 7.0 [Wol08].

The influence of component value deviations on the five stage PPF that was discussed in its ideal form in Sec. 3.4.1.2 was analyzed. The input signal to the PPF was applied in a dual-feed manner, just as in the analysis of the ideal PPF. In Fig. 3.15(a), both mean value and standard deviation of $\Delta\theta_{IQ}$ for 20000 PPFs with tolerances of 0.5 % between capacitors and 0.2 % between resistors are presented. The frequency dependence of the mean value is identical to the frequency dependence of $\Delta\theta_{IQ}$ in the ideal PPF. This is because the effect of the component value deviations averaged out. The effect of the component value deviations can instead be found in the standard deviation of $\Delta\theta_{IQ}$. For example from the standard deviation at 1 MHz, it can be

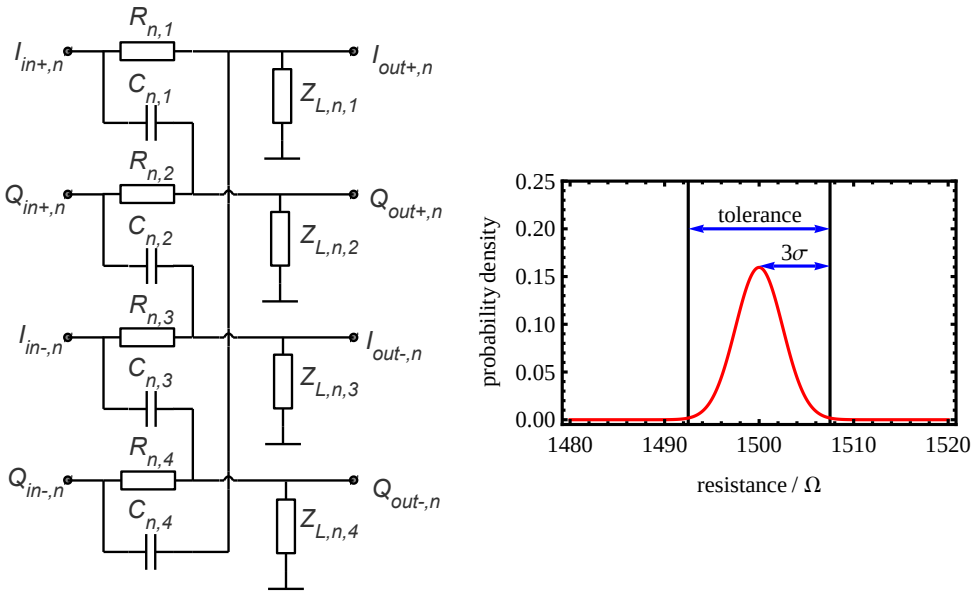

(a) n-th stage of a real PPF with deviations among the resistors, capacitors and load impedances.

(b) Assumed probability density function for a set of 1.5 kΩ resistors with a tolerance of 1 %.

Figure 3.14.: Component value deviations.

concluded that for 99.7 % (corresponding to three standard deviations) of all PPFs realized with components of these tolerances, $\Delta\theta_{IQ}$ will deviate less than ∼0.1° from $\Delta\theta_{IQ}$ in the ideal case. This means that the deviations from the ideal behaviour due to these tolerances can be on the same order of magnitude than the highest deviations of $\Delta\theta_{IQ}$ from 90° that are inherent to the PPF. The deviation of A_{IQ} from unity is not shown here, since its influence, according to Eq. (3.7), is much smaller compared to $\Delta\theta_{IQ}$ for the PPF analyzed here.

To find the tolerance at which the influence of component value deviations is negligible compared to the deviations of $\Delta\theta_{IQ}$ from 90° inherent to the PPF, the standard deviation of $\Delta\theta_{IQ}$ was calculated for different tolerances. This was done at a frequency of 1.061 MHz, the highest pole frequency of the PPF. At this frequency the standard deviation is the highest in the frequency range of interest. The tolerances of the capacitors and the resistors were identical in this analysis. The results can be found in Fig. 3.15(b). It can be seen that for a tolerance of approximately $3.5{\cdot}10^{-4}$, three standard deviations, which cover more than 99.7% of all PPFs, are one order of magnitude smaller than the highest deviation of $\Delta\theta_{IQ}$ from 90° that is inherent to the

PPF.

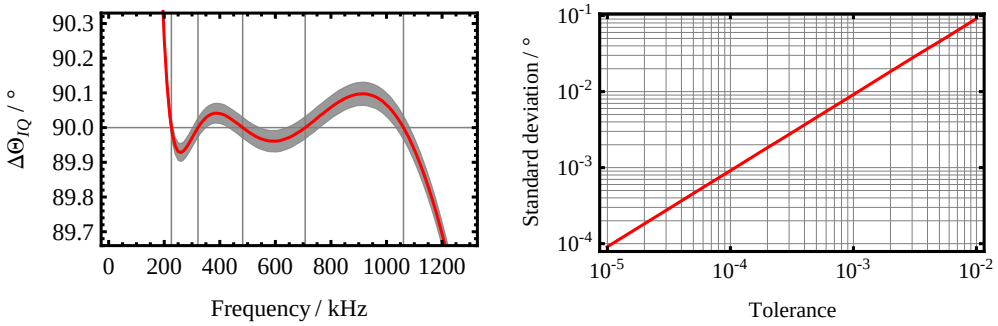

(a) Mean value, displayed by the red line, and standard deviation, displayed by the gray area, of $\Delta\theta_{IQ}$ for 20000 PPFs with tolerances of 0.5 % between capacitors and 0.2 % between resistors.

(b) Standard deviation of $\Delta\theta_{IQ}$ against tolerance for 20000 PPFs with identical tolerances for capacitors and resistors at 1.061 MHz, the highest pole frequency.

Figure 3.15.: Results of the analysis of a five stage PPF with nominal component values as the ideal PPF discussed in Sec. 3.4.1.2. The load impedances were assumed to be identical.

Load imbalance: Besides component value deviations, load imbalances, i.e. differences between the load impedances of a stage, disturb the symmetry of the PPF. Eq. (3.9) shows that an imbalance in the load of the final stage affects all stages of the PPF and not only the final stage.

The influence of load imbalances on the above introduced five stage PPF was analyzed. In the analysis, there were no component value deviations within the PPF, but the final stage was loaded by 7 pF capacitors with 10 % tolerance. At each frequency, 20000 PPFs were analyzed.

Mean value and standard deviation of $\Delta\theta_{IQ}$ are presented in Fig. 3.16(a). It can be seen that the mean value is identical to the $\Delta\theta_{IQ}$ in the ideal PPF. The standard deviation can be on the same order of magnitude as the deviation of the ideal $\Delta\theta_{IQ}$ from 90°. In Fig. 3.16(b), mean value and standard deviation of A_{IQ} are presented. The mean value is unity at all frequencies. According to Eq. (3.7), the contribution of the standard deviation of A_{IQ} to the degradation of the SSR is comparable to the contribution of the standard deviation of $\Delta\theta_{IQ}$. Both standard deviations increase significantly with increasing frequency. Therefore, the effect of an imbalanced load is more pronounced at high frequencies.

A further analysis showed that for a load imbalance of ∼1.5 %, the effect of the load imbalance on the SSR is negligible for all frequencies of interest. At this imbalance, the degradation of SSR due to the imbalanced load is more than one order of magnitude

smaller than the effect of the highest deviation of $\Delta\theta_{IQ}$ from 90° that is inherent to the PPF.

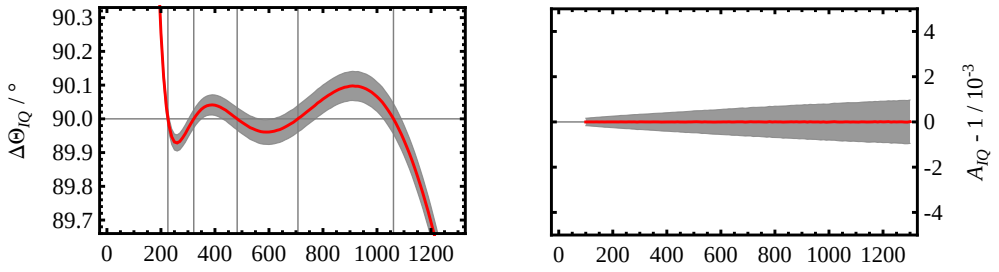

(a) $\Delta\theta_{IQ}$ (b) A_{IQ}

Figure 3.16.: Mean value and standard deviation of $\Delta\theta_{IQ}$ and A_{IQ} for 20000 realisations of a five stage PPF. The PPFs had nominal component values as the ideal PPF discussed in Sec. 3.4.1.2. There were no component value deviations, but the final stage was loaded by 7 pF capacitors with a tolerance of 10 %.

3.4.2. Realisation

Axial signals of ions in the PENTATRAP experiment will be analyzed with FFT analyzers. The axial frequency will be at about 600kHz, which is above the frequency range of FFT analyzers that meet the frequency resolution and dynamic range requirements of the experiment. Therefore, the axial signals will have to be converted into the frequency range of the FFT analyzers. For this purpose, an axial frequency amplifier with integrated down converter was designed by Stahl Electronics [Sta10]. With respect to the influence of the down conversion on the SNR of the axial signal, an important feature of the design is that it provides single sideband down conversion. The theory behind the down converter was presented in Sec. 3.4.1. Part of the work for this thesis was to set up, optimize and characterize this down converter.

In the course of the optimization of the first version AF-DC-b of the down converter, potential for improvement of the sideband suppression was found. This resulted in a change of the layout and a second version named AF-DC-c [Sta10].

3.4.2.1. Setup

AF-DC-b/c uses two parallel JFETs and an operational amplifier as pre-amplifier stage. The 90° phase shift between the two local oscillator signals is introduced by a five stage PPF. The mixers SA612AD [Phi97] are integrated circuits (ICs) containing

a Gilbert cell for the down conversion process. The sum frequency components of the mixer outputs are removed by low-pass filters. The 90° phase shift at intermediate frequency is carried out by a six stage PPF. The subtraction of the two IF signals is performed by a differential amplifier. The maximum and minimum pole frequencies of the PPFs determine the maximum IF and LO frequency ranges, in which the down converter is applicable. For IF, the range reaches from 2.1 kHz to 21.2 kHz. For ν_{LO}, the range reaches from 226 kHz to 1061 kHz. A picture of the final configuration of AF-DC-c can be found in Fig. 3.17.

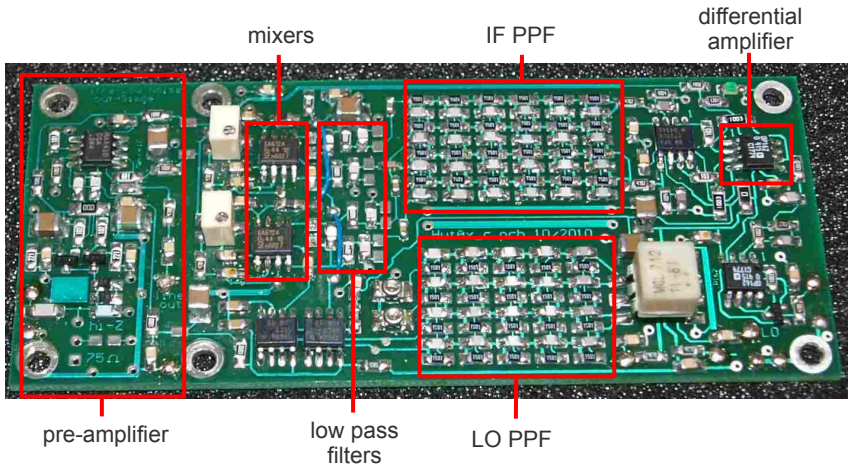

Figure 3.17.: Final configuration of the axial frequency amplifier with integrated down converter AF-DC-c [Sta10]. The pre-amplifier and the components relevant for the sideband suppression are labeled.

The components for the two PPFs were preselected with an Agilent E4980A LCR meter with a HP 16034E test fixture for surface-mounted devices (SMD). The components for the first version AF-DC-b were pre-selected with accuracies on the order of 10^{-3} to 10^{-4}. For the pre-selection of the components of the second version, the influence of component value deviations on the accuracy of the 90° phase shift provided by the PPFs was calculated. The results of this calculation for the five stage LO-PPF were presented in Sec. 3.4.1.2. It was shown that for components with tolerances less than $3.5{\cdot}10^{-4}$, the maximum deviation of the phase shift from 90° due to the component value deviations is at least one order of magnitude smaller than the maximum deviation inherent to the PPF. The same holds for the IF-PPF. Therefore the components of the PPFs of AF-DC-c were pre-selected with an accuracy goal of $3.5{\cdot}10^{-4}$. Other components that influenced the symmetry of the PPFs were pre-selected with an accuracy on the same order of magnitude. The relative differences between the pre-selected resistors and capacitors that were used in AF-DC-c can be found in App. A.

3.4.2.2. Sideband suppression

Measurement of the sideband suppression: A test setup was assembled to measure and optimize the sideband suppression of AF-DC-b/c. A schematic of this setup is shown in Fig. 3.18. The measurement procedure to obtain the sideband suppression at a local oscillator frequency f_{LO} and an intermediate frequency IF was the following: The LO signal generator produced a sine wave at the frequency f_{LO}. The input signal generator was first set to generate a sine wave at the frequency $f_{LO} + IF$ (upper sideband), then to generate one at the frequency $f_{LO} - IF$ (lower sideband). In both cases, the output amplitudes at IF were measured with the FFT analyzer. From the two output amplitudes, the sideband suppression ratio was calculated.

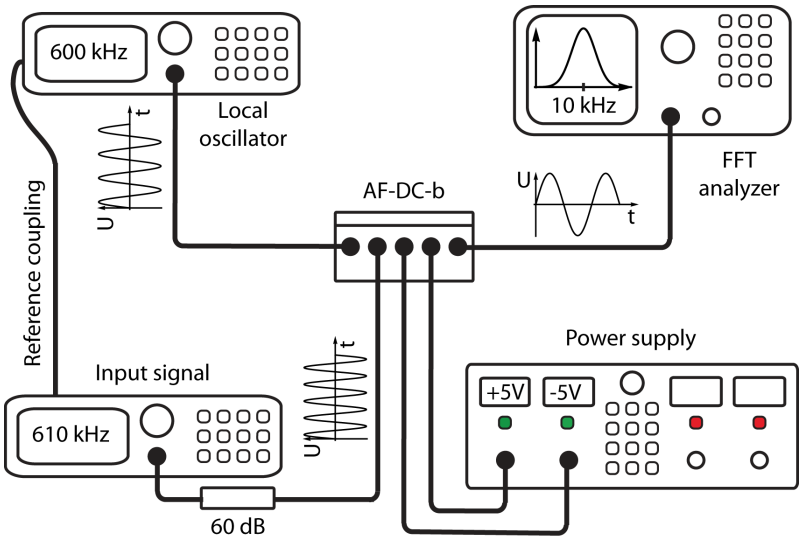

Figure 3.18.: Setup for the measurement of the sideband suppression. An aluminium box with BNC feedthroughs shielded the down converter from HF noise. The input signal and the local oscillator signal were provided by two Agilent 33250A function generators. To prevent relative frequency drifts over time, they were coupled via the reference input of the one and the reference output of the other. To reach input amplitudes comparable to the input amplitudes in the experiment, the signal of the corresponding function generator was attenuated by 60 dB. The power supply was a HAMEG HM 7044. The sideband amplitudes were measured with a HP 35670A FFT analyzer.

Load balancing: The load balance of the final stage of a PPF can have a major influence on the sideband suppression performance (see Sec. 3.4.1.2). In the course of the optimization of the first down converter version AF-DC-b the load configuration of

the LO-PPF was changed. The initial and the final load configuration of the LO-PPF are shown in Fig. 3.19(a) and Fig. 3.19(b), respectively. The changes from the intial to the final configuration of AF-DC-b resulted in an improvement of the sideband suppression on the order of 20 dB.

In Sec. 3.4.1.2, it was shown that the load of the LO-PPF has to be balanced with an accuracy better than 1.5 % to make the reduction of the sideband suppression ratio due to the load imbalance one order of magnitude smaller than the reduction that is inherent to the PPF. In the second version AF-DC-c, the two 7 pF capacitors in Fig. 3.19(b) were replaced by two 3-10 pF trimming capacitors (see Fig. 3.19(c)). These trimming capacitors allow for an easy adjustment of the load balance to an accuracy of 1.5% or better.

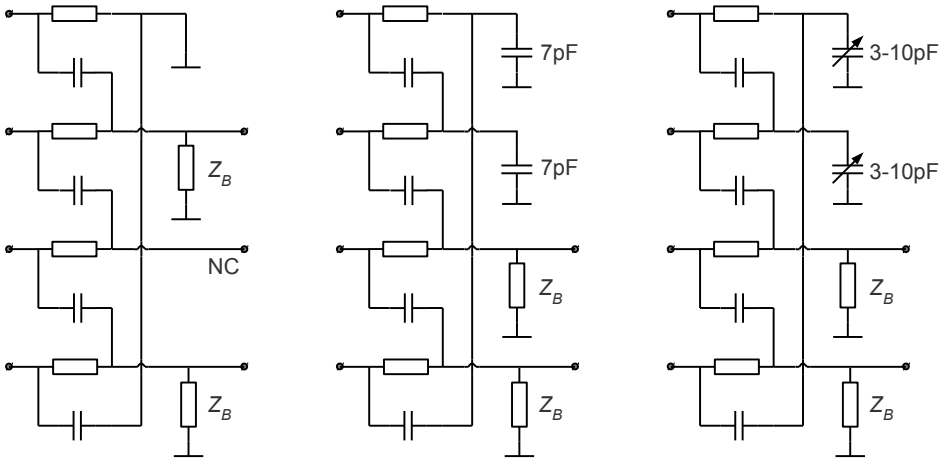

(a) Initial configuration of AF-DC-b. Two outputs are connected to impedance transformers, one is grounded and one is not connected.

(b) Final configuration of AF-DC-b. The connection from the PPF to the impedance transformers was changed and two 7 pF capacitors improve the load balance.

(c) Configuration of AF-DC-c. Two trimming capacitors allow for a fine tuning of the load balance.

Figure 3.19.: Different load configurations for the final stage of the LO-PPF. The impedances Z_B are the input impedances of the two impedance transformers following the LO-PPF. In the ν_{LO} range of AF-DC-b/c, Z_B is determined by the input capacitance of typically 8 pF [Bur96].

Mixers: The transfer function of the mixer IC used in the down converter has a low-pass characteristic, i.e. for a fixed LO frequency, the output signal amplitude

decreases with increasing IF. Differences in the low-pass characteristics of the two mixers in the down converter can limit the sideband suppression. This is illustrated in Fig. 3.20: In Fig. 3.20(a), the transfer functions of two mixers with different low pass characteristics are shown. When these mixers are incorporated into a single sideband down converter, the sideband suppression shown in Fig. 3.20(b) is obtained. Except for a small IF range around the distinct peak, the sideband suppression is limited to rather low values of 30 dB and less.

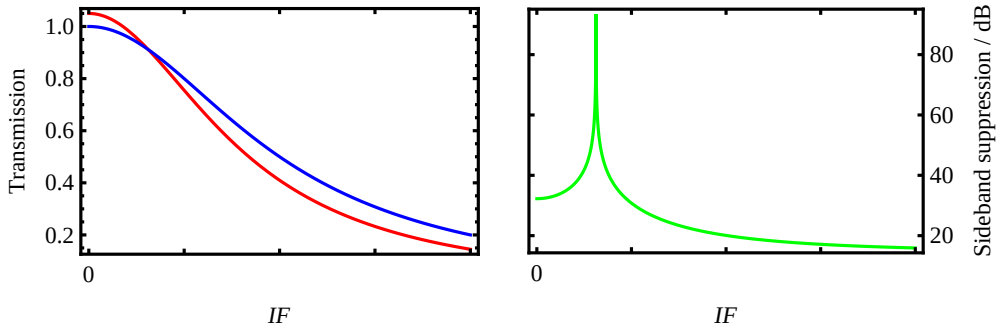

(a) Transfer functions of two mixers with different low-pass characteristics. One of the mixers has a slightly higher conversion gain. Transmissions are normalized to the DC transmission of one of the mixers.

(b) Resulting sideband suppression, i.e. ratio of constructive and destructive superposition of the mixer output signals. Equal input signal amplitudes for both mixers were assumed.

Figure 3.20.: Transfer functions of two mixers with different low-pass characteristics and the resulting sideband suppression for the mixers being incorporated into a single sideband down converter are shown.

In fact, this behaviour was observed for the AF-DC-b. Therefore, a test setup resembling the environment of the mixer ICs in the down converter was assembled. A schematic of the setup is shown in Fig. 3.21. It has to be noted that each mixer has two outputs. With the test setup, the transfer functions of both outputs of a mixer were determined.

The amplitude of one output of a mixer for different IF is presented in Fig. 3.22, together with a corresponding fit. In the fit model, both mixer outputs were treated as low-pass filters with transfer functions like simple RC low-passes. The outputs were followed by the low-passes included in the test setup. The resulting fit function was given by:

$$f(\nu) = \frac{A_{\mathrm{DC}}}{\sqrt{1+\nu^2/\nu_{\text{-3dB}}^2}\sqrt{1+\nu^2\cdot(2\pi\cdot 680\ \Omega\cdot 2.2\ \mathrm{nF})^2}}, \tag{3.10}$$

where A_{DC}, the DC amplitude, and $\nu_{\text{-3dB}}$, the cutoff frequency, were the fit parameters.

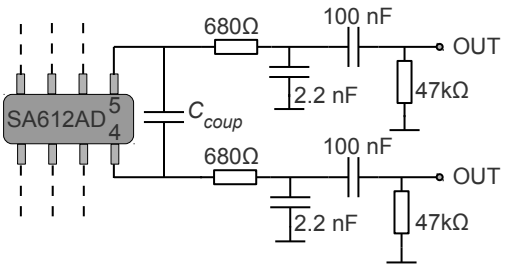

Figure 3.21.: Test setup for mixers. The setup resembles the environment of a mixer IC in the down converter. For reasons of clarity, only the components which are connected to the two outputs of the mixer are shown. At a LO frequency of 600 kHz, the output amplitudes were measured for input signals of fixed amplitude with different input frequencies $\nu_{LO} - IF$. As voltage supply, LO signal generator, input signal generator and FFT analyzer, the same devices as in the setup for the sideband suppression measurement were used. Different coupling capacitors C_{coup} between the mixer outputs were used in the test measurements.

The cutoff frequency one received from the fit shown in Fig. 3.22 was $\nu_{\text{-3dB}} = 17022.7$ Hz with the 95 %-confidence interval given by $[16953.5, 17091.8]$ Hz.

For one mixer, the cutoff frequencies were measured for different values of C_{coup}. The result is shown in Fig. 3.23. It can be seen that the cutoff frequency continuously decreases with increasing C_{coup}. From this, it was concluded that different values of C_{coup} can be used to compensate for different low-pass characteristics of two different mixers. In fact, a 15 % higher coupling capacitance between the ouputs of one mixer in AF-DC-b resulted in sideband suppression improvement of 5 dB and more.

The mixers for AF-DC-c were pre-selected. The mixer test setup described above with a coupling capacitance of C_{coup}=4.7 nF was used to characterize the outputs of 65 mixers. For all mixers, the cutoff frequencies $\nu_{\text{-3dB}}$ of the two mixer outputs agreed within the 95 %-confidence intervals of each other. In the case of the DC amplitudes A_{DC}, this was the case only for 55 % of the mixers. Between the mixers, these parameters varied on scales much larger than the widths of the confidence intervals. The minimum value of $\nu_{\text{-3dB}}$ of all mixer outputs was 9269 Hz, whereas the maximum value was 10560 Hz. A_{DC} varied between 8.45 mV_{rms} and 9.32 mV_{rms}. The two mixers chosen for the first realisation of AF-DC-c have the properties shown in Tab. 3.4.

Performance: Fig. 3.24 shows the sideband suppression of AF-DC-c for different intermediate frequencies at a fixed local oscillator frequency of 600 kHz. For IF between 3 kHz and 23 kHz, the sideband suppression is between 56 dB and 77 dB. For most frequencies it is above 60 dB. The positions of the peaks that can be seen

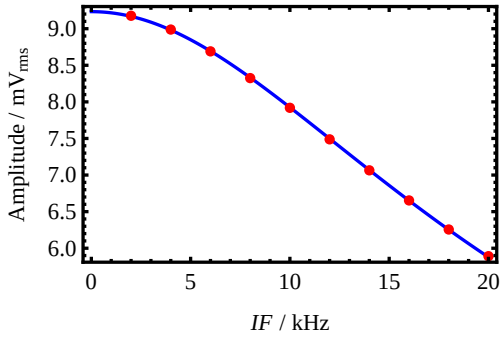

Figure 3.22.: Amplitude at one output of a mixer in the test setup against IF (C_{coup}=2.2 nF). The red dots indicate the measured points and the blue line the fit of Eq. (3.10) to the points. Error bars are smaller than the size of the dots.

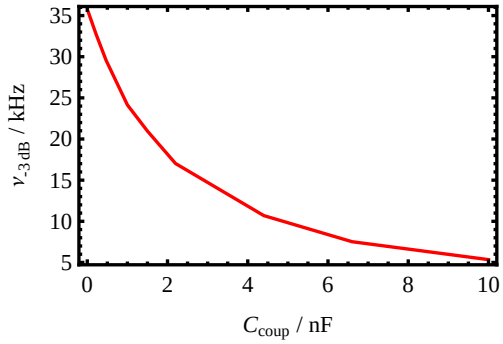

Figure 3.23.: Cutoff frequency $\nu_{\text{-3dB}}$ against C_{coup} for one output of a mixer in the test setup.

Mixer	Output	A_{DC} / mV$_{rms}$	$\nu_{\text{-3dB}}$ / Hz
1	1	8.870±0.031	10308±80
	2	8.868±0.030	10302±77
2	1	8.835±0.030	10312±76
	2	8.834±0.030	10307±75

Table 3.4.: DC amplitude A_{DC} and cutoff frequency $\nu_{\text{-3dB}}$ of both outputs in the test setup for the two mixers used in the first realisation of AF-DC-c.

in the spectrum do not coincide with the pole frequencies of the IF-PPF. Therefore it can be concluded that the peaks are not related to the phase shift provided by the IF-PPF. Most probably, they arise from slight differences in the cutoff frequencies between the low pass characteristics of the mixer outputs. These differences could be between the outputs of a single mixer as well as between the outputs of two mixers. As the sideband suppression is on a level, where the degradation of the SNR due to noise from the unwanted sideband is negligible compared to the degradation of the SNR due to the pre-amplifier's noise (see below), no attempt was made to compensate these differences.

In Fig. 3.25, it can be seen that the sideband suppression at a fixed intermediate frequency of 10 kHz is between 55 dB and 68 dB for local oscillator frequencies between 250 kHz and 1.1 MHz. Therefore, the down converter is applicable in principle over a wide axial frequency range.

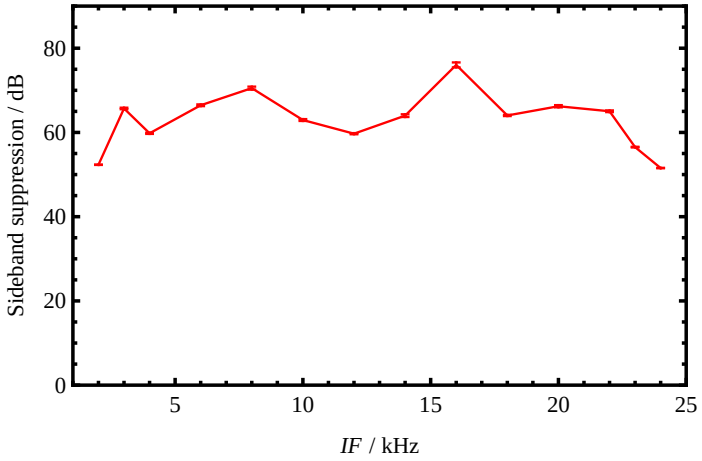

Figure 3.24.: Sideband suppression against intermediate frequency for a fixed local oscillator frequency of 600 kHz.

3.4.2.3. Gain and voltage-noise density of the pre-amplifier

The noise of an amplifer is usually described by equivalent noise sources [TS02]: All noise in the amplifier is referred to two noise sources at the input of the amplifier, a voltage noise source U_n and a current noise source I_n. The amplifier itself is assumed to be noise free. A sketch of this model is shown in Fig. 3.26.

As the current noise density of the pre-amplifier was specified to be 20 fA/$\sqrt{\text{Hz}}$ [Sta10] and the output impedance of the preceding amplifier in the PENTATRAP experiment will be ∼50 Ω, the current noise was assumed to be negligible. Therefore, only the voltage-noise density was measured. Noise spectra were measured with a Rohde & Schwarz ZVL spectrum analyzer. To lift the noise of the pre-amplifier above

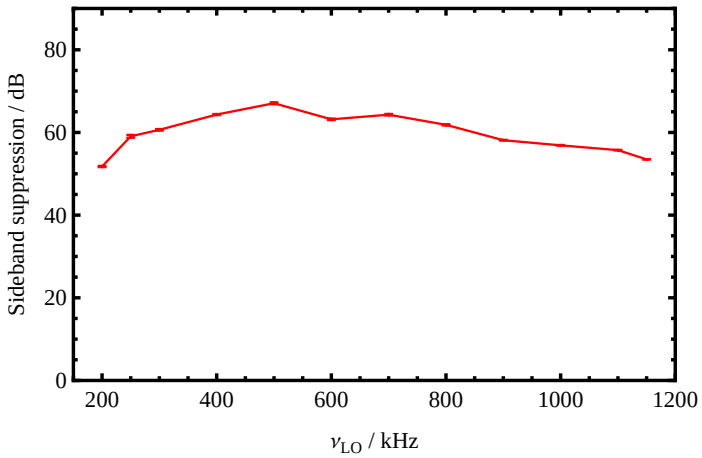

Figure 3.25.: Sideband suppression against local oscillator frequency for a fixed intermediate frequency of 10 kHz.

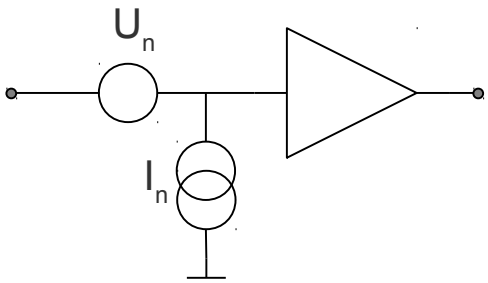

Figure 3.26.: Amplifier with equivalent voltage and current noise sources U_n and I_n, respectively.

the noise at the input of the ZVL, an additional low-noise amplifier (LNA) was used. Gains were measured with a HP 4195A network analyzer. The following measurements were performed to obtain the voltage-noise density of the AF-DC-c pre-amplifier:

- Gain $G_{\mathrm{PA}}(\nu)$ of the pre-amplifier.
- Gain $G_{\mathrm{LNA}}(\nu)$ of the LNA.
- Noise spectrum $U_{\mathrm{LNA}}(\nu)$ of the LNA. This included the input noise of the spectrum analyzer.
- Noise spectrum $U_{\mathrm{PA}}(\nu)$ of the pre-amplifier - LNA cascade. The pre-amplifier was shunted at the input.

Since the noise of the AF-DC-c pre-amplifer, the noise of the LNA and the noise of

the ZVL were uncorrelated, the voltage-noise density was calculated as follows:

$$u_{\mathrm{PA}}(\nu) = \frac{\sqrt{|U_{\mathrm{PA}}(\nu)|^2 - |U_{\mathrm{LNA}}(\nu)|^2}}{G_{\mathrm{LNA}}(\nu) \cdot G_{\mathrm{PA}}(\nu) \cdot \sqrt{\Delta\nu}}, \tag{3.11}$$

where $\Delta\nu$ was the measurement bandwidth.

In Fig. 3.27, the voltage-noise density of the AF-DC-c pre-amplifier is shown. Since the amplitudes of the distinct peaks that can be seen in the spectrum were reduced when the shielding of the setup was improved, these peaks are most likely due to external noise. The voltage-noise density of the AF-DC-c pre-amplifier is less than 0.75 $\mathrm{nV}/\sqrt{\mathrm{Hz}}$ for frequencies between 200 kHz and 1 MHz. The gain of the AF-DC-c pre-amplifier is shown in Fig. 3.28. It is ∼33 dB in the same frequency range.

As the voltage-noise density of the cryogenic amplifier is ∼0.8 $\mathrm{nV}/\sqrt{\mathrm{Hz}}$ at a frequency of 600 kHz, and provides a gain >10 dB, the AF-DC-c pre-amplifier increases the noise background by less than 30 %.

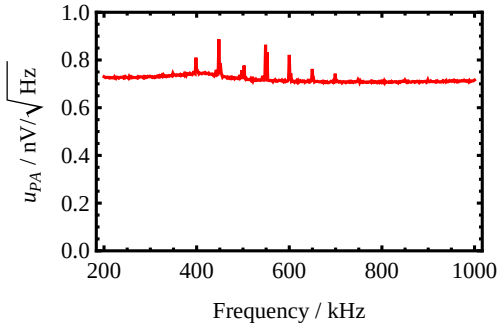

Figure 3.27.: Spectrum of the voltage-noise density u_{PA} of the AF-DC-c pre-amplifier.

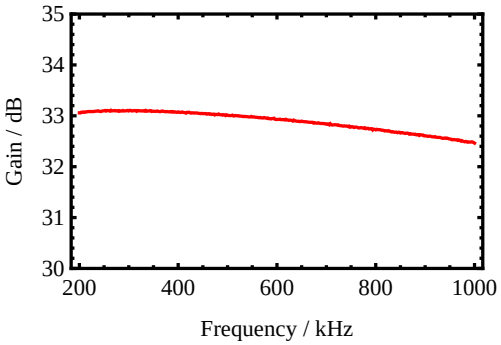

Figure 3.28.: Gain of the AF-DC-c pre-amplifier against the signal frequency.

3.5. Test of the axial detection system

The axial detection system was assembled to prove that it works in principle. The axial resonator and the axial amplifier were cooled to ∼4 K. White noise was capacitively coupled to the resonator. The resonator signal was amplified by the cryogenic axial amplifier, converted to lower frequencies by the AF-DC-c and detected by an FFT. A schematic of the setup is shown in Fig. 3.29.

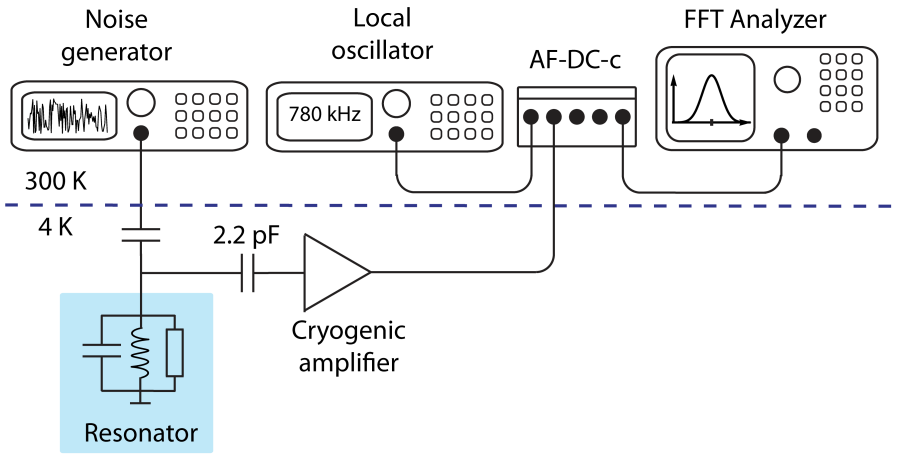

Figure 3.29.: Setup for the test of the axial detection system. The axial resonator and the cryogenic axial amplifier were placed in a cryostat and cooled by a cryocooler. The resonator is represented by the LCR circuit it forms intrisically. Noise generated by an Agilent 33250A function generator was coupled to the resonator with a small capacitance. The cryogenic amplifier was coupled to the resonator with a 2.2 pF capacitor. The amplifier output was amplified and converted to lower frequencies by the AF-DC-c. The local oscillator signal for the AF-DC-c was generated by an Agilent 33250A function generator as well. The output of the down converter was detected with a HP 35670A FFT analyzer. Voltage supplies for the cryogenic amplifier and the down converter are omitted in the schematic for reasons of clarity.

The resonance of the resonator was found at ∼ 790 kHz. Therefore, the LO frequency was chosen to be 780 kHz. The full resonance, as measured with the FFT, is shown in Fig. 3.30(a). The solid line depicts a Lorentzian curve that was fitted to the data. From the fit, a resonance frequency of 9291.5±0.7 Hz and a quality factor of 2791±13 was deduced.

For a comparison between the signal before and after the down converter, the resonance was also measured behind the cryogenic axial amplifier with a Rohde & Schwarz ZVL spectrum analyzer. The result of this measurement, together with the

Lorentzian fitting curve, is shown in Fig. 3.30(b). From the fit, a resonance frequency of 789288.5±0.9 Hz and a quality factor 2794±18 was found. This is in good agreement with the values that were found for the down converted resonance, if one takes the LO frequency of 780 kHz into account.

It can be seen that the quality factor in both cases is more than an order of magnitude below the quality factor of the axial resonator shown in Tab. 3.1. This has probably two reasons: First of all, some windings had to be removed from the toroid, as they had been cut accidentally, which reduced the free quality factor. Furthermore, the input impedance of the axial amplifier might have been insufficiently decoupled by the 2.2 pF capacitor, so that it decreased the quality factor. A later measurement, carried out by Christian Roux, in fact gave a quality factor of ∼35000 when the axial amplifier was coupled to the resonator with only 0.3 pF [Rou11b].

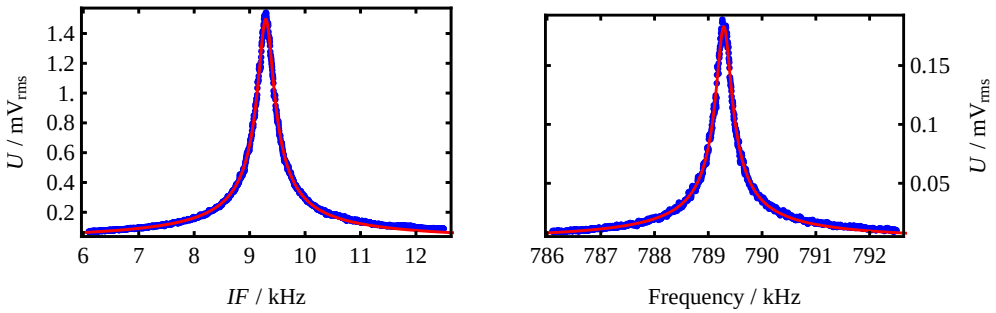

(a) Resonance behind the down converter, measured with an FFT analyzer. The solid line depicts the Lorentzian fit function.

(b) Resonance after the cryogenic axial amplifier, measured with a spectrum analyzer. The solid line depicts the Lorentzian fit function.

Figure 3.30.: Resonance of the axial resonator.

4. SQUIDs

The axial frequency of ions in the PENTATRAP experiment will be ∼600 kHz. At this frequency, 1/f noise contributes with several 100 pV/$\sqrt{\text{Hz}}$ to the total voltage noise density of the cryogenic axial amplifier (for details, see [Rou11a]). Amplifiers based on superconducting quantum interference devices (SQUIDs) have 1/f corner frequencies far below the axial frequency. Commercially availabe SQUIDs based on low temperature superconductors have 1/f corner frequencies on the order of 0.1 Hz [Fag06].

Therefore, a SQUID based axial amplifier might be used in the PENTATRAP experiment. To the knowledge of the author, there is only one Penning trap experiment so far that has employed a SQUID for the detection of an ion's axial eigenmotion [WLB+88].

SQUIDs are highly sensitive magnetic flux-to-voltage transformers. They are used as magnetometers with field resolutions up to the level of 10^{-17}T [Fag06]. Furthermore, they can be employed for the detection of any signal that can be converted to a magnetic flux. A SQUID basically consists of a superconducting ring, containing usually either one or two weak links. These weak links, which are called Josephson junctions, are discussed in Sec. 4.1.1. The ring might either consist of a low-temperature superconductor (LTS) or a high-temperature superconductor (HTS). SQUIDs with one Josephson junction are so-called RF SQUIDs, where the RF indicates that a radio frequency signal is inductively coupled into the superconducting ring [ZTH70]. DC SQUIDs contain two Josephson junctions in parallel, biased with a direct current [JLSM64]. Most commercialy available SQUIDs are DC SQUIDs [Fag06]. They will be discussed in Sec. 4.1.2.

4.1. Theory of SQUIDs

4.1.1. Josephson junctions

A Josephson junction consists of two weakly coupled superconductors. The coupling, which is based on tunneling processes, can be realized in manifold ways, e.g. by connecting two superconductors with a small layer of insulating or normal conducting material or by a microbridge [Fag06].

4.1.1.1. Josephson equations

Due to their bosonic nature, the Cooper pairs in a superconductor condense in a collective ground state, the BCS ground state, which can be described by the following

wave function [Hun09]:

$$\Psi(\vec{r}) = \sqrt{n_s} e^{i\varphi(\vec{r})}, \tag{4.1}$$

where n_s is the Cooper pair density and $\varphi(\vec{r})$ is the phase. The static probability current density of a particle of mass M and charge q is given by [CTDL77]:

$$\vec{J}(\vec{r}) = \frac{1}{M} \mathrm{Re}\left\{ \Psi^*(\vec{r}) \left[\frac{\hbar}{i} \vec{\nabla} - q\vec{A}(\vec{r}) \right] \Psi(\vec{r}) \right\}, \tag{4.2}$$

where $\vec{A}(\vec{r})$ is a vector potential. With charge $q = -2e$ and mass $M = 2m_e$ of a Cooper pair, assuming a homogeneous Cooper pair density throughout the superconductor, one derives from Eq. (4.1) and Eq. (4.2) the following expression for the supercurrent density:

$$\vec{j}_s(\vec{r}) = -\frac{e\hbar n_s}{m} \left(\vec{\nabla}\varphi(\vec{r}) - \frac{2\pi}{\Phi_0} \vec{A}(\vec{r}) \right), \tag{4.3}$$

where $\Phi_0 = \frac{h}{2e} \approx 2 \cdot 10^{-15}$ Tm^2 is the so-called flux quantum. Introducing the gauge invariant phase $\delta(\vec{r}) = \varphi(\vec{r}) - \frac{2\pi}{\Phi_0} \int_0^{\vec{r}} \vec{A} d\vec{s}$, this can be written as

$$\vec{j}_s(\vec{r}) = -\frac{e\hbar n_s}{m} \vec{\nabla}\delta(\vec{r}). \tag{4.4}$$

If a weak link is introduced into the superconductor, there are two regions of high Cooper pair density connected by a thin region with strongly reduced Cooper pair density. But the Cooper pairs are still in a collective ground state $\Psi(\vec{r})$. For a supercurrent to flow through the Josephson junction, the supercurrent density has to be the same throughout the junction. Therefore, the reduced Cooper pair density in the weak link has to be compensated by a large gradient of the gauge invariant phase $\delta(\vec{r})$. For a given Cooper pair density and a given thickness of the weak link, the suppercurrent through a Josephson junction is fully characterized by the difference of the gauge invariant phases δ_1 and δ_2 at the two superconductor - weak link boundaries [BK04]:

$$I_s = I_s(\gamma), \tag{4.5}$$

where $\gamma = \delta_2 - \delta_1 = \varphi_2 - \varphi_1 - \frac{2\pi}{\Phi_0} \int_1^2 \vec{A} d\vec{s}$ is the gauge invariant phase difference. $I_s(\gamma)$ should be invariant under changes of γ which are multiples of 2π. Due to the non-dissipative flow of Cooper pairs, it should furthermore be invariant under time reversal. Therefore, $I_s(\gamma)$ can be expanded in a series of sine functions [BK04]. Assuming that all terms of the series but the first one are neglectable, one finds the first Josephson equation:

$$I_s(\gamma) = I_c \sin(\gamma), \tag{4.6}$$

where I_c is the critical current, i.e. the maximum supercurrent, the junction can carry.

The second Josephson equation relates the time derivative of the gauge invariant phase difference to the voltage drop U over the Josephson junction [CB04]:

$$\dot{\gamma} = \frac{2\pi}{\Phi_0} U. \tag{4.7}$$

U arises from different energies of the Cooper pairs in the two superconductors ($\dot{\varphi}_2 - \dot{\varphi}_1$) and from induced voltages ($\frac{2\pi}{\Phi_0} \int_1^2 \dot{\vec{A}} d\vec{s}$).

4.1.1.2. RCSJ model

In the "resistively and capacitively shunted junction" model (RCSJ model) [Ste68], the real Josephson junction is modeled as a point-like ideal Josephson junction in parallel with the junction's self-capacitance C and a linear resistance R. The ideal Josephson junction is characterized by its critical current I_c. R is the junction's resistance in parallel to a shunt resistor that might have been introduced to remove hysteresis from the current-voltage characteristic of the junction. The thermal noise of R is represented in the model by a current noise source I_n. A junction in the RCSJ model is presented in Fig. 4.1. The time-averaged voltage drop over the junction is denoted by U in this figure.

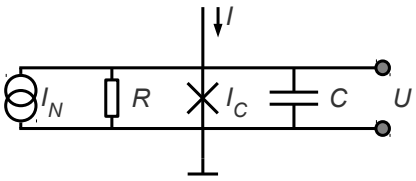

Figure 4.1.: A Josephson junction in the "resistively and capacitively shunted junction" model, biased by a current I [Ste68]. The two crossed lines in the middle represent the ideal Josephson junction.

The RCSJ model does not only take into account supercurrents, which are related to the critical current of the junction I_c and the gauge invariant phase difference γ via the first Josephson equation. It also includes quasiparticle currents U/R and displacement currents, which are given by $C\dot{U}$. Neglecting the current noise source and using the second Josephson equation to express U in terms of the time derivative of the gauge invariant phase difference, one derives the following differential equation for the gauge invariant phase difference [Ste68]:

$$\frac{\Phi_0}{2\pi} C\ddot{\gamma} + \frac{\Phi_0}{2\pi} \frac{1}{R} \dot{\gamma} = I - I_c \sin\gamma. \tag{4.8}$$

A characteristic quantity of a Josephson junction in the RCSJ model is the so-called Stewart-McCumber parameter β_c [McC68]:

$$\beta_c = \frac{2\pi}{\Phi_0} I_c R^2 C. \tag{4.9}$$

In the limit $\beta_c \ll 1$, which is called the strongly overdamped limit, the solution of Eq. (4.8) yields the relation between the bias current I and the time-averaged voltage U across the Josephson junction shown in Fig. 4.2. For $I<I_c$, the voltage across the junction is zero and the current is completely carried by Cooper pairs. For $I>I_c$, where the voltage across the junction is non-zero, both time-dependent currents of quasiparticles and Cooper pairs carry the bias current. With increasing bias current, the time-averaged supercurrent is steadily decreasing and the current-voltage relation becomes more and more ohmic. When the thermal noise of R is taken into account, the steep edge in the current voltage relation at the critical current is rounded.

For a non-negligible Stewart-McCumber parameter, the current-voltage relation becomes hysteretic, i.e. the course of the time averaged voltage depends on whether the bias current is increased or decreased. To remove hysteresis, resistive shunts across the junction are used [TC77]. In this case, the RCSJ model reduces to the "resistively shunted junction" (RSJ) model.

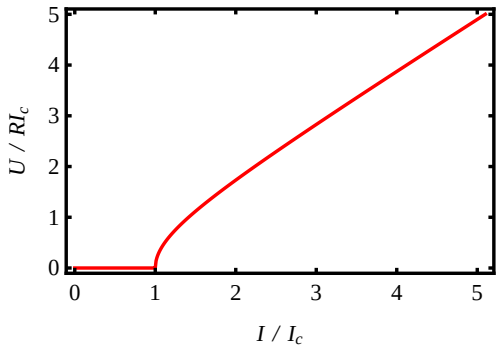

Figure 4.2.: Time-averaged voltage across the Josephson junction against bias current in the strongly overdamped limit of the RCSJ model [CB04].

4.1.2. DC SQUIDs

4.1.2.1. Basics

A DC SQUID consists of a superconducting ring, containing two Josephson junctions in parallel, which are biased with a DC current [JLSM64]. A schematic of a SQUID with Josephson junctions in the RSJ model is shown in Fig. 4.3 [TC77]. The schematic also contains the inductances of the two SQUID arms.

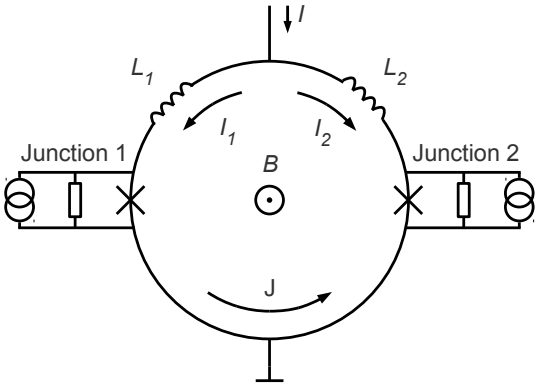

Figure 4.3.: DC SQUID with Josephson junctions according to the RSJ model [TC77]. L_1 and L_2 indicate the inductances of the two SQUID arms. I is the bias current, I_1 is the current along the left SQUID arm, I_2 the one along the right arm and J the current circulating around the SQUID ring. B indicates an external magnetic flux pointing into the plane of this page.

The equations of motion of the gauge invariant phase differences γ_1 and γ_2 are left unaltered in comparison to the case of a single junction. But as the junctions are incorporated into the same superconducting ring, γ_1 and γ_2 are not independent. It can be found from integration of the phase of the Cooper pair wave function along the SQUID ring, that the two gauge invariant phase differences are related as follows [BK04]:

$$\gamma_2 - \gamma_1 = \frac{2\pi}{\Phi_0}(\Phi_a + LJ), \tag{4.10}$$

where L is the total inductance of the SQUID ring and Φ_a is the total external flux coupled into the SQUID ring (indicated in Fig. 4.3 by the magnetic field B).

For negligible inductances, it is convenient to introduce the auxiliary quantity $\gamma \equiv \gamma_1 + \pi\frac{\Phi_a}{\Phi_0} = \gamma_2 - \pi\frac{\Phi_a}{\Phi_0}$. The equation of motion of γ is of the same form as the equation of motion of the gauge invariant phase difference in a Josephson junction, with the only difference that the critical current is modulated by the external flux: $I_c \propto \cos(\pi\frac{\Phi_a}{\Phi_0})$ [CB04]. Therefore, the current voltage relation of the DC SQUID is of the same form as the relation for the Josephson junction, just with a critical current that is modulated by an external flux with a period of Φ_0. This is shown in Fig. 4.4.

From Fig. 4.4, it can be seen that for a bias current that is larger than or equal to the flux dependent critical current, a change of the external flux leads to a change of the time-averaged voltage. This is the basis of all DC SQUID applications: Either the SQUID is directly used to measure magnetic fluxes, or a quantity is transformed into a flux, which is then coupled into the SQUID. For example, an RF signal can be coupled

inductively to the SQUID ring with an input coil. This way, the SQUID can be used as an RF amplifier [HC85]. In any case it is favorable that a SQUID is operated in a manner, that a change of the external flux leads to a maximum voltage change.

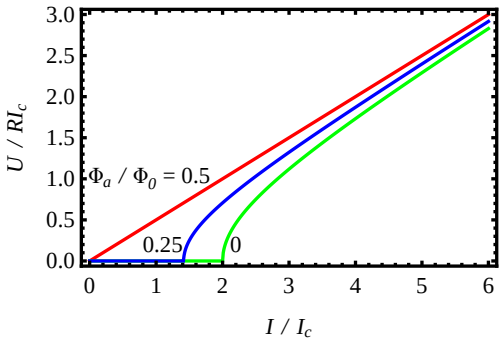

Figure 4.4.: Time-averaged voltage against bias current for a DC SQUID with identical Josephson junctions and neglectable inductances for three different external fluxes [CB04]. The Josephson junctions are described in the RSJ model.

The thermal noise of the Josephson junctions' resistances R leads to a rounding of the current-voltage relation of the SQUID, just as in the case of the Josephson junctions. This rounding removes the divergence of $\partial U/\partial\Phi$ at the critical current. Without the divergences, a reasonable SQUID transfer function can be defined [CB04]:

$$U_\Phi = \max\left(\left|\frac{\partial U}{\partial \Phi_a}\right|\right). \tag{4.11}$$

A practical SQUID has a finite inductance L. Otherwise, external flux cannot be coupled to the SQUID. The inductance reduces the modulation of the critical current. The modulation of the voltage with the external flux is therefore reduced as well [BK04].

A relation between external flux and time-averaged voltage across the SQUID in the presence of noise for a DC SQUID with non-negligible inductance parameter is shown in Fig. 4.5 for illustration purposes. The sinusoidal form resembles the form of the flux-voltage-characteristic of many real DC SQUIDs [CB04]. To a SQUID with such a relation, one would usually apply a bias flux of $(\mathrm{n}+\frac{1}{4})\Phi_0$ to set the working point to the steepest part of the curve. The straight line crossing the curve at Φ_a=1.25Φ_0 has a slope corresponding to the transfer function of the SQUID.

4.1.2.2. Flux locked loop SQUID operation

From Fig. 4.5, it can be seen that the linear range of the Φ_a-U relation is limited to a fraction of a flux quantum. To increase the dynamic range, SQUIDs are often

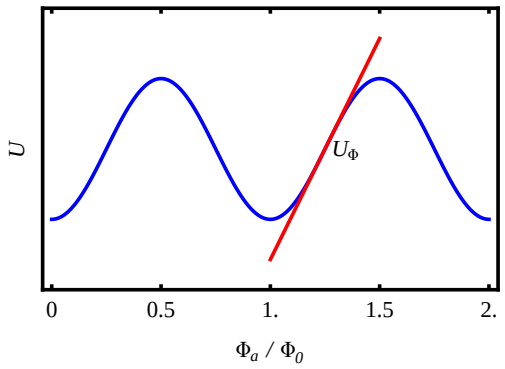

Figure 4.5.: Time-averaged voltage against external flux for a DC SQUID with non-negligible inductances in the presence of noise. The straight line is to indicate the working point and the transfer function of the SQUID.

operated in a so-called flux locked loop (FLL) [Dru03]. A simplified schematic of an RF amplifier using a SQUID in FLL mode is shown in Fig. 4.6.

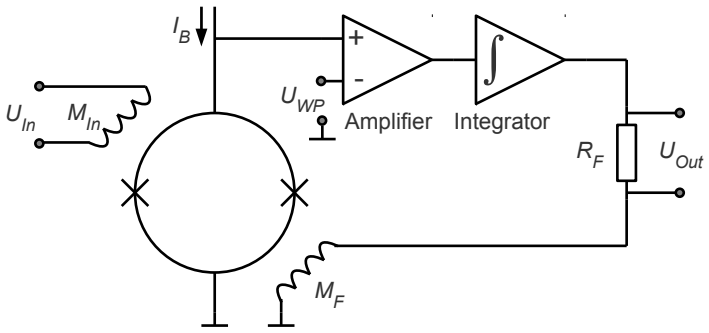

Figure 4.6.: Schematic of a SQUID in a flux locked loop. The SQUID is biased by a DC current I_B. The working point on the Φ_a-U-curve is set by the bias voltage U_{WP}. The voltage across the junction is compared to U_{WP} with a differential amplifier. The output of this amplifier is then integrated. The integrator gives an error signal that is both read out and fed back to the SQUID loop with a feedback resistor of resistance R_F and a feedback coil with mutual inductance M_F. An RF signal can be applied to the SQUID through an input coil so that the SQUID can be used as an RF amplifier.

To set the working point on the Φ_a-U-relation, the SQUID is biased with a current I_B and the voltage at the working point is applied as a reference to one input of a

differential amplifier. The voltage across the SQUID is applied to the other input of the amplifier. The integrator behind the differential amplifier integrates the difference between these two voltages over time. Its output is used as an error signal, which is fed to the SQUID with a feedback resistor and a feedback coil. The setup is adjusted such that the feedback flux keeps the total flux through the SQUID ring at the flux of the working point. An RF signal can be coupled to the SQUID through an input coil. In this case, the error signal serves for two purposes: First of all, it keeps the transfer function constant, even for large flux changes. Secondly, the error signal is a measure for the applied flux. It therefore serves as the output of the RF amplifier.

4.2. First experimental results

In this section, results of first experimental steps with a DC SQUID will be presented.

A sensor was provided by the working group "Cryosensors" at the Physikalisch-Technische Bundesanstalt Berlin. The SQUID is made from niobium with 4 µm wide Al_2O_3 junctions. A carrier for the sensor chip and a niobium capsule were bought from Magnicon GmbH [Mag11a]. The niobium capsule is suitable for the shielding from both external noise and weak static magnetic fields. The SQUID was controlled and read out by the Magnicon SQUID electronics XXF-1 [Mag10].

Purpose of the first tests, which were proposed in the XXF-1 manual [Mag10], was to observe basic features of the SQUID and to learn about its handling. For these tests, the SQUID in the niobium capsule was placed in a cryostat and cooled down by a cryocooler. Twisted pair copper wires were used for the connection to the XXF-1 SQUID electronics. The electronics was controlled by the Magnicon SQUIDViewer software [Mag11b].

Current-voltage relation: The relation between the bias current I_B and the voltage U across the SQUID was measured. To do so, a bias current sweep was performed with the internal function generator of the XXF-1 SQUID electronics. Both U, amplified by the XXF-1, and the reference signal of the function generator were detected with an oscilloscope. A schematic of the measurement setup can be found in Fig. 4.7. For I_B between 0 and 10 μA_{pp}, the I_B-U relation shown in Fig. 4.8 was obtained. This can be compared with the I_B-U relation of a noiseless SQUID shown in Fig. 4.4. Due to thermal noise, the relation is rounded around the critical current. The critical current I_c in this relation is given by $\sim$5 µA. In the measurement of the flux-voltage relation, that will be presented in the next paragraph, it was observed that 5 µA is not the maximum critical current of the SQUID. Therefore, it can be concluded that the SQUID ring was threaded by an external magnetic flux during the measurement of the I_B-U relation.

Flux-voltage relation: To obtain the relation between the flux Φ through the SQUID ring and the voltage U across it, the SQUID was biased with a current I_B and a flux

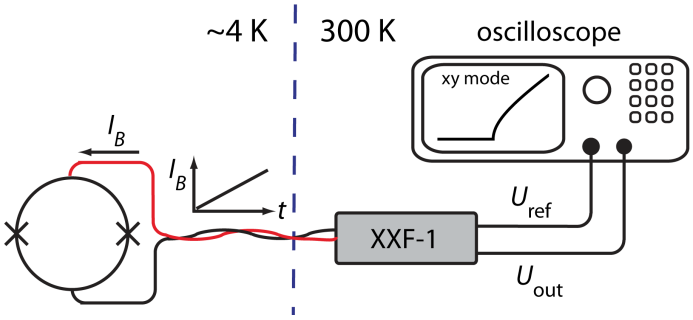

Figure 4.7.: Schematic of the setup for the measurement of the I_B-U relation of the SQUID. The SQUID is placed in a cryostat and cooled down by a cryo-cooler. A pair of twisted copper wires provides the connection for the bias current and the voltage read-out between the SQUID and the XXF-1 electronics. The internal function generator of the XXF-1 is used for a bias current sweep. A MSO2024 oscilloscope detects both the output signal U_{out} of the XXF-1 and the reference signal of the function generator U_{ref}. The computer controlling the electronics is omitted for reasons of clarity.

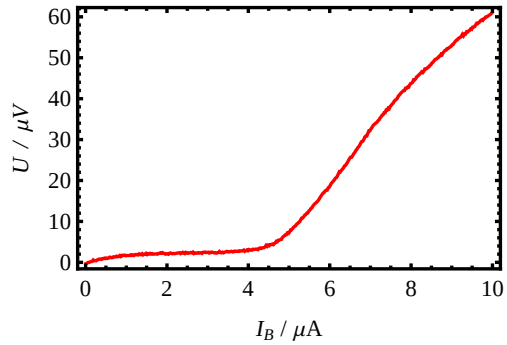

Figure 4.8.: Relation between bias current I_B and voltage U across the SQUID.

sweep was performed. This was done with the internal function generator of the XXF-1. A schematic of the measurement setup is shown in Fig. 4.9. The result of this measurement is shown in Fig. 4.10. It can be seen, that the Φ-U relation is asymmetric, i.e. the rising edge is steeper than the falling edge. This increases the transfer function of the SQUID for operation at the rising edge.

The maximum modulation of U was achieved for a bias current of I_B=9.8 µA. This is significantly higher than the critical current $I_c \approx$5 µA obtained from the I_B-U relation shown in Fig. 4.8. As the maximum modulation is usually achieved for a bias current slightly above the maximum critical current of the SQUID, this means that the critical current in Fig. 4.8 is not the maximum critical current. Therefore, it can be concluded

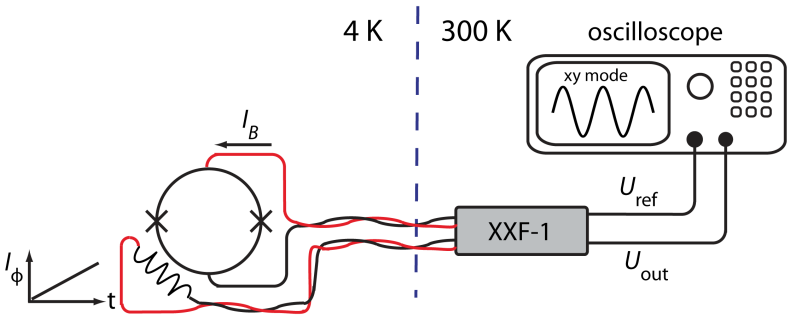

Figure 4.9.: Schematic of the setup for the measurement of the Φ-U relation of the SQUID. The SQUID is placed in a cryostat cooled down by a cryocooler. A pair of twisted copper wires is used to apply a current I_Φ with the XXF-1 to the feedback coil. This results in an additional flux through the SQUID ring. Another pair of twisted copper wires is used to bias the SQUID and to read out the voltage across it. The internal function generator of the XXF-1 is used to perform a flux sweep. A MSO2024 oscilloscope detects both the output signal U_{out} of the XXF-1 and the reference signal of the function generator U_{ref}. The computer controlling the electronics is omitted for reasons of clarity.

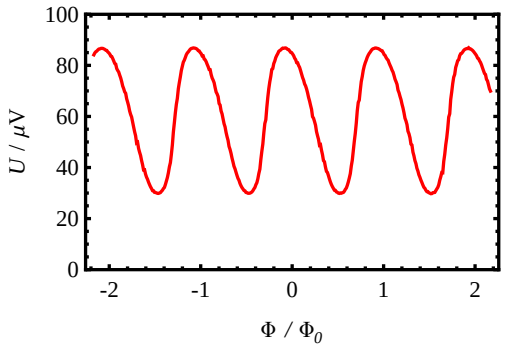

Figure 4.10.: Relation between the externally applied flux Φ and the voltage U across the SQUID. The flux is normalized to a flux quantum Φ_0. The SQUID was biased by a current of I_B=9.8 µA. This resulted in a maximum modulation of U.

that the SQUID ring was threaded by an external flux during the measurement of the I_B-U relation.

Setup of the SQUID for FLL mode: The purpose of the last measurement was to find the settings of the SQUID for the operation in a flux-locked loop. First, the bias current for which the Φ-U relation has the steepest rising edge was determined: While I_B was varied, the Φ-U relation was observed with the oscilloscope. The steepest rising edge was found at I_B=9.4 µA. The XXF-1 in FLL mode locks to zero voltage U_{out} at the differential amplifier output [Mag10]. Therefore, the bias voltage U_B at the reference input of the amplifier in the XXF-1 had to be determined, for which the working point, i.e. the steepest part of the Φ-U relation, is at U_{out}=0 V. This was the case for U_B=54.4 µV. These settings resulted in the Φ-U relation shown in Fig. 4.11. The gray lines indicate the working point of the SQUID. The blue line represents a linear fit to the relation around the working point. From the fit, a transfer function of U_Φ=367.6 µV/Φ_0 with a 95 %-confidence interval of [360.7, 374.5] µV/Φ_0 was obtained.

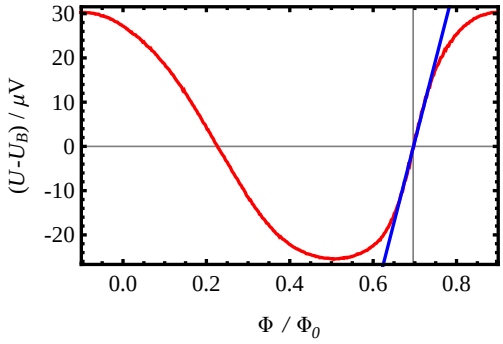

Figure 4.11.: Φ-U relation for the settings that were found to be optimal for the operation of the SQUID in a flux locked loop. The gray lines mark the working point of the SQUID in FLL mode. The slope of the blue line is the transfer function of the SQUID.

5. Magnetic shielding in a strong and homogeneous magnetic field

A SQUID is very sensitive to changes of the magnetic flux through the SQUID ring. Therefore, a SQUID that is operated in a high magnetic field has to be shielded from this field. In this section, possible realisations of a magnetic shield in the magnet of the PENTATRAP experiment are presented. Furthermore, as the homogeneity of the magnetic field in the trap region is crucial for the precision of mass measurements in the PENTATRAP experiment, the influence of a magnetic shield on the homogeneity of the field is investigated.

5.1. Magnetic shielding in a strong magnetic field

The shield will be placed in a region of the magnet, where the magnetic flux density is 1 T and more. Conventional shielding with a material of high susceptibility is not possible at these fields: To obtain best shielding, the magnetic flux density has to be sufficiently far away from the saturation field strength of the material. For mu-metal, e.g., the maximum magnetic flux density that can be shielded is 200 mT [SPS87].

For shields in strong magnetic fields, superconductors can be employed. The shielding with a superconductor can either be based on the expulsion of a magnetic field from the superconductor or on the conservation of magnetic flux through a closed superconducting loop.

Superconductors are classified into type-I and type-II superconductors, depending on the response of a bulk sample of the superconductor to an external magnetic field. A type-I superconductor completely expels magnetic fields up to its critical field B_c. This is the the so-called Meißner-Ochsenfeld effect [BK04]. For fields $B > B_c$, the sample becomes normal conducting. A type-II superconductor completely expels magnetic fields up to its lower critical field $B_{c,1}$, as well. But the superconducter stays in the superconducting state for fields $B > B_{c,1}$, as long as B does not exceed the upper critical field $B_{c,2}$. For field strengths between $B_{c,1}$ and $B_{c,2}$, an external field is not completely expeled from the superconductor. It can penetrate the superconductor and is partially damped.

To the knowledge of the author, there is no superconductor that is able to expel fields of 1 T and more. A superconducting shield based on the expulsion of the magnetic field therefore has to be of onion-like structure: One or more outer layers made from a type-II superconductor have to damp the field step by step, until the field is low

enough to be completely expelled by the innermost layer.

Another shielding technique employs the conservation of magnetic flux through a closed superconducting loop. A hollow superconducting cylinder conserves the flux directed along its symmetry axis that was applied when the cylinder underwent the phase transition from the normal conducting to the superconducting state. If this flux is zero, the inner of the cylinder is shielded from any fields directed along the symmetry axis. The maximum field strength that can be shielded is determined by two factors: The strength of the field has to be below the upper critical field of the superconductor. Furthermore, the cylinder has to be thick enough so that the density of the shielding currents does not exceed the critical current density of the superconductor. Recently, it was demonstrated that a hollow MgB_2 cylinder of height 70 mm, with an inner diameter of 18 mm and an outer diameter of 35.5 mm, is able to completely shield its bore from axial fields with a strength of up to 2 T [ROB+10].

5.2. Magnetic shielding in a homogeneous magnetic field

When a magnetic shield is placed in a magnetic field, the field induces a magnetization in the shield. The field that is arising from this magnetization is superimposed on the initial field and changes the field configuration. Purpose of this section is to estimate the influence of a magnetic shield on the homogeneity of the magnetic field in the trap region of the PENTATRAP experiment.

In the first paragraph of this section a simple formula for the magnetization of an ideal (ellipsoidal) shield in a homogeneous magnetic field will be derived. Furthermore, it will be demonstrated that for a shield sufficiently far from the magnetic field region of interest, the magnetic field arising from the magnetization of the shield can well be approximated by the field of a magnetic dipole with the total magnetic moment of the shield. This approximation, together with the formula for the magnetization, will then be used in the second paragraph to estimate the influence of a magnetic shield on the homogeneity of the field of the PENTATRAP magnet.

Magnetization and magnetic field: In the following, a shield that is brought into an initially homogeneous magnetic field of flux density $\vec{B}_0$ is considered. It is assumed that the shielding works perfectly, i.e. the magnetic flux density in the shielded volume is zero. Therefore, a susceptibility of -1 is assigned to the shielded volume: The shield behaves as an ideal diamagnet. Although a pracitical shield might rather be of cylindrical shape, the shield is assumed to be of prolate ellipsoidal shape, i.e. it is football shaped. This assumption simplifies the calculations, as the field of a homogeneously magnetized ellipsoid, in contrast to that of homogeneously magnetized cylinder, can be analytically calculated [Cha61]. In fact, it is common practice in the field of micromagnetics to replace cylindrical objects by equivalent ellipsoids [BGM06]. The equivalence of, e.g., an elongated cylinder and a prolate ellipsoid with symmetry axes along the

same direction and identical homogeneous magnetization densities is established by equal volumina and identical demagnetization coefficients along the symmetry axes.

For the magnetic flux density inside a diamagnet, the following relation holds:

$$\vec{B} = \mu_0(\vec{H} + \vec{M}) = 0, \tag{5.1}$$

where μ_0 is the vacuum permeability, $\vec{H}$ is the total magnetic field inside the shield volume and $\vec{M}$ is the magnetization density. $\vec{H}$ is the sum of the initial magnetic field $\vec{H}_0$ and the field $\vec{H}_m$ that is arising from the magnetization of the shield:

$$\vec{H} = \vec{H}_0 + \vec{H}_m. \tag{5.2}$$

$\vec{H}_m$ is related to the magnetization density $\vec{M}$ as follows [Aha00]:

$$\vec{H}_m = -\underline{\underline{D}}\vec{M}, \tag{5.3}$$

where $\underline{\underline{D}}$ is the so-called demagnetization tensor. Without loss of generality, it is assumed that the axes of the coordinate frame coincide with the major and the minor axes of the prolate ellipsoid, so that the demagnetization tensor is diagonal. In this case, Eq. (5.3) reduces to:

$$H_{m,i} = -D_i M_i, \tag{5.4}$$

where i=x, y, z. From Eq. (5.1), Eq. (5.2) and Eq. (5.4), it can be deduced that in this case the magentization density is related to the strength of the initial field as follows:

$$M_i = -H_{0,i}\frac{1}{1 - D_i}. \tag{5.5}$$

The demagnetization coefficient of the ellipsoid along the symmetry axis, which is assumed in the following to coincide with the $\hat{e}_z$-axis, is only determined by the aspect ratio τ_e of the ellipsoid, i.e. the ratio of the lengths of the major and the minor axis [BGM06]:

$$D_z(\tau_e) = \frac{1}{1 - \tau_e^2}\left[1 - \frac{\tau_e \arccos(\tau_e)}{\sqrt{1 - \tau_e^2}}\right]. \tag{5.6}$$

The other two demagnetization coefficients are identical, since the axes perpendicular to the symmetry axis are interchangeable. As the trace of the demagnetization tensor is always unity, they are given by [BGM06]:

$$D_{x,y}(\tau_e) = \frac{1}{2}(1 - D_z(\tau_e)). \tag{5.7}$$

With Eq. (5.5), (5.6) and (5.7), the magnetization density for prolate ellipsoids of arbitrary volume and arbitrary aspect ratio can be calculated.

In the following, the field outside of a diamagnetic prolate ellipsoid arising from the magnetization of the ellipsoid in a homogeneous magnetic field is compared to the field

of a magnetic dipole with the same magnetic moment as the ellipsoid. The formulae for the calculation of the field of the ellipsoid were taken from [Cha61]. The field of the magnetic dipole moment was calculated as follows [Jac62]:

$$\vec{B}(\vec{r}) = \frac{\mu_0}{4\pi}\left(\frac{3\hat{r}(\hat{r}\vec{m}) - \vec{m}}{|\vec{r}|^3} - \frac{8\pi}{3}\vec{m}\delta(\vec{r})\right), \tag{5.8}$$

where $\hat{r} = \vec{r}/|\vec{r}|$ is the normalized distance vector and $\vec{m}$ is the magnetic dipole moment.

The results for an ellipsoid of aspect ratio five with the external field directed along the symmetry axis of the ellipsoid are presented in Fig. 5.1. (a) shows the deviation from unity of the ratio between the field components in the axial direction, i.e. in the direction of the external magnetic field, and (b) the same quantity for the radial field components. For the axial components, the deviation is less than 8 % for all axial distances larger than twice the length of the ellipsoid l and all radial distances. The deviation is constantly decreasing with the axial distance and is less than 1 % for distances larger than 5.5 l. The radial dependence of the deviation is rather weak for most distances. For the radial component, the deviation is less than 10 % for all axial distances larger than 2.3 l and smaller than 1 % for distances larger than 7 l. The radial dependence of the deviation for this component is even weaker.

In Fig. 5.2, these deviations are presented for different aspect ratios of the ellipsoid. It can be seen that for small aspect ratios, the deviations strongly decrease with decreasing aspect ratio, both for the axial and the radial field component. On the other hand, for aspect ratios larger than five, the deviations do not increase significantly with increasing aspect ratio. Thus, the deviations presented in Fig. 5.1 can be seen as an upper limit.

In the case, in which the external field is directed along a minor axis of the prolate ellipsoid, the field of the magnetized shield is in even better agreement with the field of the magnetic dipole and the dependence of the deviation on the aspect ratio is similar to the case discussed before. Therefore, this case won't be discussed in detail.

The results presented here demonstrate that for distances larger than about 2.5 times the shield length, the accuracy of approximating the field of a magnetized shield by the field of its total magnetic moment is better than 10 % for all field components, independently of the relative orientation of the shield and the external field. When the influence of a magnetized shield on the homogeneity of a given field distribution is analyzed, this accuracy is sufficient to estimate the order of magnitude of the influence.

Magnetic shield in the PENTATRAP magnet: In this paragraph, the influence of an ideal, i.e. diamagnetic, shield on the homogeneity of the magnetic field of the PENTATRAP magnet is analyzed. The shield is a prolate ellipsoid of 78 mm length, with an aspect ratio of 1.89. This ellipsoid is equivalent to a cylinder with the same length and outer diameter as the hollow MgB_2 cylinder mentioned in Sec. 5.1, which shielded its bore from fields up to 2 T [ROB+10].

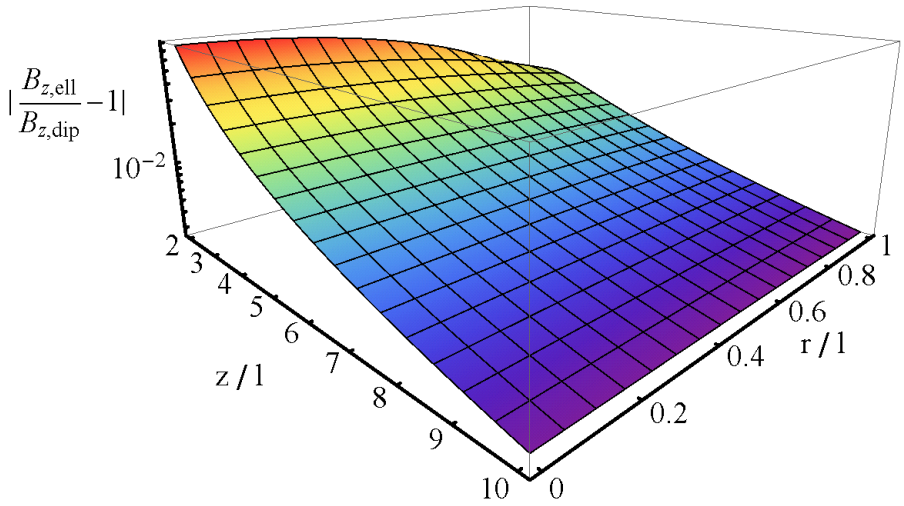

(a) Deviation from unity of the ratio $B_{z,\mathrm{ell}}/B_{z,\mathrm{dip}}$ of the axial field components, i.e. the components in the direction of the external magnetic field.

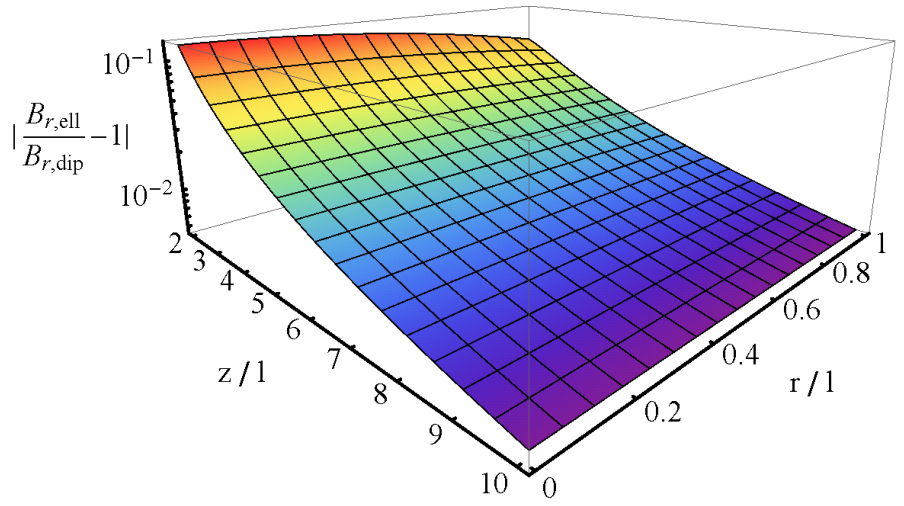

(b) Deviation from unity of the ratio $B_{r,\mathrm{ell}}/B_{r,\mathrm{dip}}$ of the radial field components, i.e. the components perpendicular to the direction of the external magnetic field.

Figure 5.1.: Deviation from unity of the ratio between the fields of a magnetized diamagnetic ellipsoid and of a magnetic dipole for different distances from the center of the ellipsoid. The ellipsoid is prolate, of length l and has an aspect ratio of five. Its magnetization is due to a homogeneous external field applied along the symmetry axis. The magnetic moment of the dipole is the same as the total magnetic moment of the ellipsoid. All distances are normalized to the length of the ellipsoid.

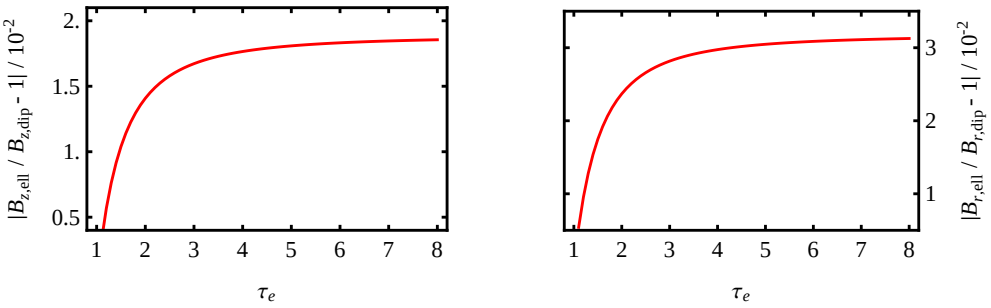

(a) Comparison of the axial field components at the axial distance 4 l and the radial distance 0.2 l.

(b) Comparison of the radial field components at the axial distance 4 l and the radial distance 0.2 l.

Figure 5.2.: Deviation from unity of the ratio between the fields of a magnetized diamagnetic ellipsoid and of a magnetic dipole against the aspect ratio of the ellipsoid. The ellipsoid is prolate and of fixed length l. Its magnetization is due to a homogeneous external field applied along the symmetry axis. The magnetic moment of the dipole is the same as the total magnetic moment of the ellipsoid.

For the calculations, the shield is placed in the magnet such, that its symmetry axis is parallel to the central axis of the magnet. The center of the ellipsoid is at a radius of 4 cm. The axial component B_z and the radial component B_r of the magnetic field of the PENTATRAP magnet at this radius for different axial distances z from the center of the magnet are presented in Fig. 5.3. The field values shown were calculated by the manufacturer of the magnet. The z range is from the bottom of the magnet to the upper limit of the helium level in the cold bore of the magnet.

From Fig. 5.3 it can be seen that for both components of the magnetic field, variations with z are up to an order of 100 mT on the scale of the shield length. To use the formalism that was derived in the last paragraph, the magnet's field in the shield volume has to be approximated by a homogeneous field. In order not to underestimate the influence of the shield, the maximum value of B_r on the axis of the ellipsoid is taken as the radial component of the homogeneous field, and the maximum value of B_z as the axial field component, respectively.

With the homogeneous field and the volume of the shield, the magnetic moment of the shield is calculated using Eq. (5.5), (5.6) and (5.7). The field of this magnetic moment, which is calculated with Eq. (5.8), is then superimposed onto the magnetic field in the center of the magnet. The field in the center of magnet was measured by Julia Repp and Alexander Rischka, using a Hall probe [Ris11].

In Fig. 5.4, the axial component of the magnetic field in the magnet's central region is displayed for three different cases: In the first case, there is no shield present in the

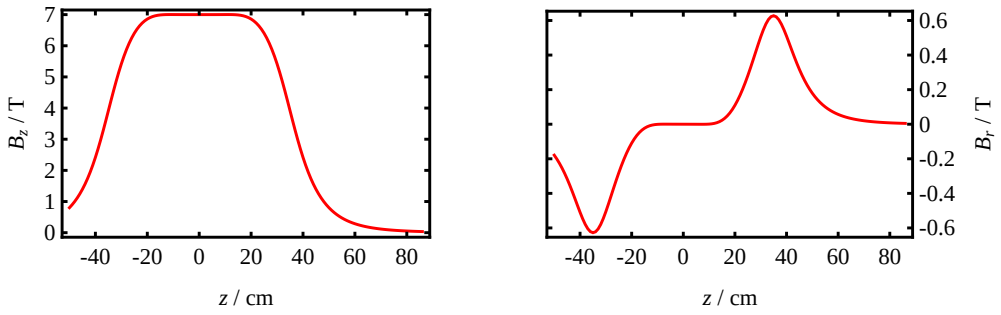

(a) Axial field component.

(b) Radial field component.

Figure 5.3.: Magnetic field components of the PENTATRAP magnet at a radius of 4 cm for different axial distances z from the center of the magnet.

magnet. The field in this case is the field as it was meaured with the Hall probe in the empty bore of the magnet. It is displayed by the upper red curve. In the second case, a shield was placed below the center of the magnet at a radius of 4 cm. In the axial direction, it was placed as far away from the center of the magnet as possible, directly above the bottom of the magnet at z_s=-46 cm. The resulting field is displayed by the blue line. The green line displays the field in the case that the shield is placed at r=4 cm and z_s=+46 cm, i.e. above the center of the magnet. It can be seen that the field change caused by the shield is quite different for the shield placed above or below the center of the trap. This is for three reasons:

- The field of a magnetic moment decays with the cubed distance. Therefore, the shield placed below the center has a bigger influence on the field at negative z in the center region, and the shield placed above the center has a bigger influence on the field at positive z in the center region.
- The radial field component is inverted under the inversion of z (see Fig. 5.3(b)). Therefore, the magnetic moments are oriented differently.
- The distance vectors from the center of the magnet to the shields are oriented differently. Therefore, the projections of the magnetic moments onto the distance vectors are different. This changes the magnetic field strength (see Eq. (5.8)).

For a more detailed analysis, polynomials of third order are fitted to the field around the trap centers of the five PENTATRAP Penning traps. The centers are marked by the vertical gray lines in Fig. 5.4. For the fits, the field values within ±12 mm around the trap centers are taken into account. Each of these intervals contains 12 datapoints. In Tab. 5.1, linear (B_1) and quadratic terms (B_2) of the magnetic field at the positions of the measurement traps 2, 3 and 4 are presented for different positions of the shield in the magnet. These three traps are of particular interest, as the actual mass-ratio measurements will be carried out in them. It can be seen, that the quadratic B_2 terms

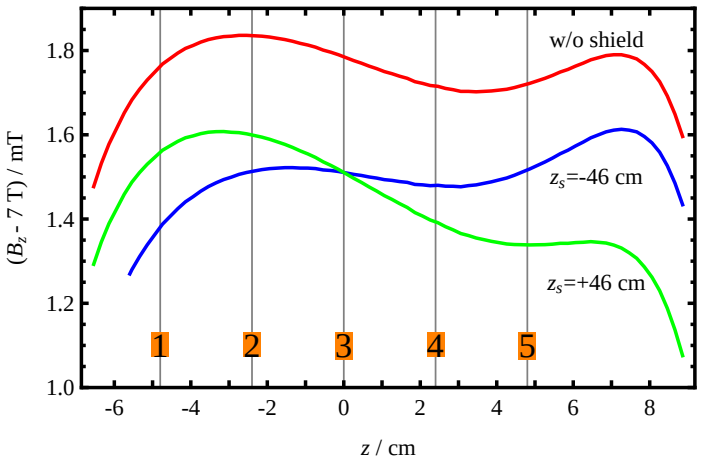

Figure 5.4.: Axial field component in the central region of the magnetic field with and without the shield present in the magnet. The upper red cure displays the field values measured in the empty bore of the magnet. The blue curve is the superposition of the measured field and the calculated field of the shield placed below the center at an axial distance of z_s=-46 cm and r=4 cm. For the green curve, the shield was placed above the center at z_s=+46 cm and r=4 cm. The vertical lines indicate the central axial positions of the five Penning traps in the PENTATRAP experiment.

for the cases in which the shield is placed at z_s=-46 cm and at z_s=+46 cm are very similar to each other. Furthermore, they do not deviate significantly from the terms in the case without a shield. The main difference between these two positions lies in the field gradient B_1, which is much higher for the shield being placed above the magnet.

To analyze the influence of the distance of the shield from the center of the magnet, the linear and quadratic terms for axial shield positions of z_s=36 cm and z_s=56 cm are determined as well (see Tab. 5.1). It can be seen, that for z_s= 36 cm, the B_1 and B_2 terms deviate significantly from the case without shield, whereas the values at z_s=56 cm are close to the case without shield. This is for two reasons: First of all, the magnetic field of a magnetic moment decreases with the cubed distance, and secondly, the shield experiences much higher B_z and B_r for z_s=36 cm, as can be seen from Fig. 5.3.

In the following, the influence of the terms B_1 and B_2 on the measurement of the eigenfrequencies of an ion in a Penning trap is discussed. The orbital momentum due to the radial motion of the ion depends on the energy of the reduced cyclotron motion E_+. The magnetic moment associated with the orbital momentum couples to the field gradient B_1 and shifts the mean position of the ion in axial direction. Therefore, the mean magnetic field experienced by the ion depends on E_+. Thus, the reduced

		Trap 2	Trap 3	Trap 4
B_1 / $\frac{\mathrm{mT}}{\mathrm{m}}$	without shield	-0.38±0.08	-3.27±0.12	-2.03±0.25
	shield at z_s=+56 cm	-0.61±0.08	-3.54±0.12	-2.35±0.25
	shield at z_s=+46 cm	-1.84±0.07	-5.06±0.12	-4.24±0.25
	shield at z_s=+36 cm	-9.29±0.08	-14.75±0.12	-17.06±0.25
	shield at z_s=-46 cm	1.84±0.08	-1.48±0.12	-0.57±0.25
B_2 / $\frac{\mathrm{mT}}{\mathrm{m}^2}$	without shield	-94.7±5.0	-19.4±7.9	67.5±16.3
	shield at z_s=+56 cm	-95.5±5.0	-20.4±7.9	66.3±16.3
	shield at z_s=+46 cm	-100.7±5.0	-27.2±7.9	57.4±16.3
	shield at z_s=+36 cm	-140.4±5.0	-82.0±7.9	-20.0±16.3
	shield at z_s=-46 cm	-104.8±5.0	-27.2±7.9	61.5±16.3

Table 5.1.: Linear and quadratic terms of the axial component of the magnetic field around the trap centers of trap 2, 3 and 4. The values are given ± the half width of 95 %-confidence interval. For more details see text.

cyclotron frequency ω_+ becomes dependent of E_+ due to the field gradient.

The quadratic field term B_2 shifts the reduced cyclotron motion in dependence of all three energies E_+, E_- and E_z [Ver04]. To compare the influence of B_1 and B_2, only the E_+ dependence is considered at first. Due to the B_2 term, a force with linear z-dependence acts on the the magnetic momentum associated with the orbital momentum of the ion. Therefore, the potential depth in axial direction is varied with E_+. As this modifies ω_z, the reduced cyclotron frequency is modified as well (see Eq. (2.4)). The ratio between the shifts $\Delta\omega_+(\Delta E_+, B_1)$ and $\Delta\omega_+(\Delta E_+, B_2)$ is given by [Ver04]:

$$\frac{\Delta\omega_+(\Delta E_+, B_1)}{\Delta\omega_+(\Delta E_+, B_2)} = \frac{B_1^2}{B_2 B_0}\left(\left(\frac{\omega_+}{\omega_z}\right)^2 - \frac{1}{2}\right). \tag{5.9}$$

For an axial frequency of ∼600 kHz and a cyclotron frequency of ∼27 MHz, the B_1 shift gives a contribution on the same order of magnitude as the B_2 shift only for the case, in which the shield is placed above the trap at z_s=+36 cm. For all other configurations listed in Tab. 5.1, the contribution is between one and three orders of magnitude smaller.

The systematic shifts of the reduced cyclotron frequency due to a non-vanishing B_2 can be summarized in a compact expression in terms of the radii r_+, r_- and

r_z [SWSB11]:

$$\frac{\delta\omega_+}{\omega_+} = \frac{B_2}{2B_0}\left(-r_+^2 + r_z^2 - r_-^2\right). \tag{5.10}$$

Here, the influence of B_2 is exemplarily discussed for a detection technique, that requires a non-thermal axial amplitude of $\sim$100 μm. It is assumed that these amplitudes cannot be reproduced exactly, but are normally distributed with a standard deviation of 10 µm. For the B_2 at the center of trap 2 in the absence of a magnetic shield, this results in an uncertainty of the cyclotron frequency determination of $(1.35\pm0.07)\cdot10^{-11}$. In the presence of the magnetic shield at z_s=-46 cm, the B_2 at the center of trap 2 results in an uncertainty of the cyclotron frequency determination of $(1.50\pm0.07)\cdot10^{-11}$. This means, that the decrease in the precision due to the shield is about one order of magnitude smaller than the decrease in the precision that arises from the B_2 that is present at the position of trap 2 without the shield.

Until this point, only the axial component of the field arising from the shield has been discussed. The radial field component was calculated to be on the order of 10 µT for $|z_s|$ larger than 40 cm. This leads to a tilt of the magnetic field on the order of 0.0001°. The shift of the cyclotron frequency due to a small tilting angle $\Theta \ll 1$ is given by [Bla06]:

$$\omega_c^{tilt} \approx \frac{9}{4}\omega_- \sin^2(\Theta). \tag{5.11}$$

For a reduced cyclotron frequency of 27 MHz and an axial frequency of 600 kHz, the magnetron frequency is given by 6.67 kHz. The radial field therefore results in relative shifts of the cyclotron frequency on the order of 10^{-15}, which are negligible.

6. Summary and outlook

Within this thesis, detection electronics for high-precision mass measurements at PENTATRAP was set up, tested and optimized.

In Chapter 3, results of test measurements with a first prototype of a Q-switch, that can be used to decouple the radial motion of the ion from the detection unit for the reduced cyclotron frequency, were presented. The GaAs switch used for this prototype proved to be unsuitable to build a Q-switch. A number of other switches will be tested soon. In the following part of this chapter, theoretical and practical issues concerning the axial frequency single sideband down converter were addressed. The influence of component value deviations and load imbalances on the accuracy of the 90° phase shift provided by the passive polyphase filters in the setup was calculated. Load imbalances were identified as a source of reduced sideband suppression in a first realization of the down converter. Compensation of these imbalances yielded an improvement of the sideband suppression on the order of 20 dB. Differences of the low-pass characteristics of the mixer outputs, which limited the sideband suppression as well, were analyzed and minimized by pre-selection of the mixers. The final characterization showed, that the voltage-noise density of the pre-amplifier increased the total noise arising from the axial amplification chain by less than 30 %. As the sideband suppression was more than 55 dB for all frequencies of interest, it can be concluded that the influence of the down conversion process on the signal-to-noise ratio is negligible compared to the amplifier noise. In the last part of this chapter, a resonance of the axial resonator was detected with all components of the axial detection system assembled. This demonstrated that the system works in principle.

The work presented in Chapter 4 and 5 was a first step towards the integration of a SQUID based axial amplifier into the setup of the PENTATRAP experiment. Results of first test measurements with a DC SQUID were presented in Chapter 4. Handling of a SQUID was demonstrated and basic properties were observed. The settings to operate the device in a flux-locked loop were determined, which is a basic prerequisite to use the SQUID as an RF amplifier. As a SQUID is highly sensitive to changes of the magnetic flux through its ring, the shielding of a SQUID in the PENTATRAP magnet was addressed in Chapter 5. Different possibilities for the practical realization of a shield were disussed. Furthermore, the influence of a shield on the homogeneity of the magnetic field in the trap region was estimated. A worst-case estimation yielded, that the shield could be placed, e.g., at the bottom of the magnet's bore without considerable disturbance of the homogeneity.

On the way to an implementation of a SQUID based axial amplifier, there are still several tasks to do. First of all, noise measurements will have to be carried out. Next,

a resonator has to be coupled to the SQUID. Furthermore, a shield has to be realized and practical problems like flux trapping during the cool-down of the shield have to be solved.

Most of the components for the PENTATRAP experiment have been machined and the assembly of the experiment is underway. The magnet is already in place and has been energized. The beam line is in place as well. The trap electrodes have been machined and gold-plated, so that the trap stack can be assembled. Most of the parts for the axial and the cyclotron resonators are available. As soon as the trap capacitances are precisely known, the axial and cyclotron coils will be wound to provide inductances corresponding to tank circuit resonance frequencies of 600 kHz and 27 MHz, respectively. Most of the cryogenic and room temperature detection electronics is available. The setup phase will be completed in the second half of this year and commissioning experiments can start.

A. Component value deviations in AF-DC-c

Part	Component	Relative difference	Uncertainty
Local oscillator passive polyphase filter	1.5 kΩ	0 - $1.3{\cdot}10^{-5}$	$4.8{\cdot}10^{-5}$
	100 pF	$0.6{\cdot}10^{-4}$	$1.4{\cdot}10^{-4}$
	150 pF	$8.2{\cdot}10^{-5}$	$9.6{\cdot}10^{-5}$
	220 pF	$9{\cdot}10^{-5}$	$6{\cdot}10^{-5}$
	330 pF	$1.0{\cdot}10^{-4}$	$0.9{\cdot}10^{-4}$
	470 pF	$7{\cdot}10^{-5}$	$3{\cdot}10^{-5}$
Intermediate frequency passive polyphase filter	7.5 kΩ	0 - $1.3{\cdot}10^{-5}$	$8.7{\cdot}10^{-5}$
	1 nF	$1.3{\cdot}10^{-4}$	$0.6{\cdot}10^{-4}$
	1.5 nF	$8{\cdot}10^{-5}$	$6{\cdot}10^{-5}$
	2.2 nF	$9{\cdot}10^{-5}$	$8{\cdot}10^{-5}$
	4.7 nF	$2{\cdot}10^{-5}$	$6{\cdot}10^{-5}$
	6.8 nF	$3{\cdot}10^{-5}$	$4{\cdot}10^{-5}$
	10 nF	$1.7{\cdot}10^{-4}$	$0.3{\cdot}10^{-4}$
C_{coup} at mixer outputs	220 pF	0	$6{\cdot}10^{-5}$
Low-pass filters behind mixer outputs	2.2 nF	$1.3{\cdot}10^{-4}$	$0.8{\cdot}10^{-4}$
	680Ω	$0.4{\cdot}10^{-4}$	$1.3{\cdot}10^{-4}$
Low-pass filters behind IF PPF	68 pF	0	$4.6{\cdot}10^{-4}$
	47 kΩ	$0.4{\cdot}10^{-4}$	$1.2{\cdot}10^{-4}$
	1 MΩ	0	$2.8{\cdot}10^{-4}$
Resistors before differential amplifier	10 kΩ	$0.1{\cdot}10^{-4}$	$1.4{\cdot}10^{-4}$
	100 kΩ	$1.0{\cdot}10^{-5}$	$8.5{\cdot}10^{-5}$

Bibliography

[Agi09] Agilent Technologies. *Agilent 35670A Dynamic Signal Analyzer Datasheet*, 2009.

[Aha00] A. Aharoni. *Introduction to the Theory of Ferromagnetism.* Oxford University Press, New York, 2000.

[BG82] L.S. Brown and G. Gabrielse. Precision spectroscopy of a charged particle in an imperfect Penning trap. *Physical Review A*, 25(4):2423–2425, 1982.

[BG86] L.S. Brown and G. Gabrielse. Geonium theory: Physics of a single electron or ion in a Penning trap. *Reviews of Modern Physics*, 58(1):233–311, 1986.

[BGM06] M. Beleggia, M.D. Graef, and Y.T. Millev. The equivalent ellipsoid of a magnetized body. *Journal of Physics D: Applied Physics*, 39:891–899, 2006.

[BH08] K. Blaum and F. Herfurth. *Trapped charged particles and fundamental interactions*, volume 749. Springer, Berlin, Heidelberg, 2008.

[BK04] W. Buckel and R. Kleiner. *Supraleitung. Grundlagen und Anwendungen.* Wiley-VCH, Weinheim, 2004.

[Bla06] K. Blaum. High-accuracy mass spectrometry with stored ions. *Physics Reports*, 425(1):1–78, 2006.

[Bur96] Burr-Brown Corporation. *BUF634 - 250mA HIGH-SPEED BUFFER*, 1996.

[CB04] J. Clarke and A.I. Braginski. *The SQUID Handbook,Vol. I.* Wiley-VCH, Weinheim, 2004.

[CBB+04] J.R. Crespo López-Urrutia, J. Braun, G. Brenner, H. Bruhns, C. Dimopoulou, I.N. Draganić, D. Fischer, A.J. González Martínez, A. Lapierre, V. Mironov, R. Moshammer, R. Soria Orts, H. Tawara, M. Trinczek, and J. Ullrich. Progress at the Heidelberg EBIT. In *Ninth International Symposium on Electron Beam Ion Sources and Traps*, Journal of Physics: Conference Series 2, pages 42–51, 2004.

[CDMU99] J.R. Crespo López-Urrutia, A. Dorn, R. Moshammer, and J. Ullrich. The Freiburg Electron Beam Ion Trap/Source Project FreEBIT. *Physica scripta*, T80:502–503, 1999.

[Cha61] H. Chang. Fields external to open-structure magnetic devices represented by ellipsoid or spheroid. *British Journal of Applied Physics*, 12:160–163, 1961.

[CTDL77] C. Cohen-Tannoudji, B. Diu, and F. Laloë. *Quantum mechanics*, volume 1.

Wiley-VCH, New York, 1977.

[CWB+89] E.A. Cornell, R.M. Weisskoff, K.R. Boyce, R.W. Flanagan Jr, G.P. Lafyatis, and D.E. Pritchard. Single-ion cyclotron resonance measurement of $M(CO^+)/M(N_2^+)$. *Physical Review Letters*, 63(16):1674–1677, 1989.

[Deh68] H.G. Dehmelt. Radiofrequency Spectroscopy of Stored Ions I: Storage*. *Advances in Atomic and Molecular Physics*, 3:53–72, 1968.

[DRE] DREEBIT GmbH. *Dresden EBIT3*.

[Dru03] D. Drung. High-Tc and low-Tc dc SQUID electronics. *Superconductor Science and Technology*, 16:1320–1336, 2003.

[DW68] H.G. Dehmelt and F.L. Walls. "Bolometric" Technique for the rf Spectroscopy of Stored Ions. *Physical Review Letters*, 21(3):127–131, 1968.

[Fag06] R.L. Fagaly. Superconducting quantum interference device instruments and applications. *Review of Scientific Instruments*, 77:101101, 2006.

[Gab09] G. Gabrielse. Why Is Sideband Mass Spectrometry Possible with Ions in a Penning Trap? *Physical Review Letters*, 102(17):172501, 2009.

[GCB+05] A.J. González Martínez, J.R. Crespo López-Urrutia, J. Braun, G. Brenner, H. Bruhns, A. Lapierre, V. Mironov, J. Scofield, R. Soria Orts, H. Tawara, M. Trinczek, and J. Ullrich. State-Selective Quantum Interference Observed in the Recombination of Highly Charged $Hg^{75+...78+}$ Mercury Ions in an Electron Beam Ion Trap. *Physical Review Letters*, 94(20):203201, 2005.

[GFGV00] M. Galeazzi, F. Fontanelli, F. Gatti, and S. Vitale. End-point energy and half-life of the ^{187} Re β decay. *Physical Review C*, 63(1):014302, 2000.

[GHR89] G. Gabrielse, L. Haarsma, and S.L. Rolston. Open-endcap Penning traps for high precision experiments. *International Journal of Mass Spectrometry and Ion Processes*, 88(2-3):319–332, 1989.

[GKT80] Gräff, G., H. Kalinowsky, and J. Traut. A Direct Determination of the Proton Electron Mass Ratio. *Zeitschrift für Physik A*, 297:35–39, 1980.

[HC85] C. Hilbert and J. Clarke. DC SQUIDs as Radiofrequency Amplifiers. *Journal of Low Temperature Physics*, 61:263–280, 1985.

[Hun09] S. Hunklinger. *Festkörperphysik*. Oldenbourg Verlag, München, 2009.

[Jac62] J.D. Jackson. *Classical Electrodynamics*. John Willey & Sons, New York, London, Sydney, 1962.

[JLSM64] R.C. Jaklevic, J. Lambe, A.H. Silver, and J.E. Mercereau. Quantum interference effects in josephson tunneling. *Physical Review Letters*, 12(7):159–160, 1964.

[KL93] R.K. Kirschman and J.A. Lipa. Further evaluation of GaAs FETs for cryogenic readout. In *Proceedings of SPIE*, volume 1946, page 350, 1993.

[KSRH08] J. Kaukovuori, K. Stadius, J. Ryynänen, and K. Halonen. Analysis and Design of Passive Polyphase Filters. *IEEE Transactions on Circuits and*

Systems I: Regular Papers, 55(10):3023–3037, 2008.

[Mag10] Magnicon GmbH. *High Performance dc SQUID Electronics XXF-1*, 2010.

[Mag11a] Magnicon GmbH. *SQUID Packaging and Wiring*, 2011.

[Mag11b] Magnicon GmbH. *SQUIDViewer*, 2011.

[McC68] D.E. McCumber. Effect of ac Impedance on dc Voltage-Current Characteristics of Superconductor Weak-Link Junctions. *Journal of Applied Physics*, 39(7):3113–3118, 1968.

[NAC+10] A. Nucciotti, C. Arnaboldi, G. Ceruti, E. Ferri, C. Kilbourne, S. Kraft-Bermuth, B. Margesin, G. Pessina, E. Previtali, D. Schaeffer, et al. The first phase of the MARE project in Milano. *Nuclear Instruments and Methods in Physics Research A*, 617(1-3):509–510, 2010.

[Pat09] D. Patranabis. *Principles of Electronics Instrumentation*. Prentice-Hall of India Pvt. Ltd, New Delhi, 2009.

[Phi97] Philips Semiconductors. *SA612A - Double-balanced mixer and oscillator*, 1997.

[RBC+11] J. Repp, Ch. Böhm, J.R. Crespo López-Urrutia, A. Dörr, S. Eliseev, S. George, M. Goncharov, Yu. Novikov, C. Roux, S. Sturm, S. Ulmer, and K. Blaum. PENTATRAP: A novel cryogenic multi-Penning trap experiment for high-precision mass measurements on highly charged ions. Submitted to Appl. Phys. B, 2011.

[RBD+11] C. Roux, Ch. Böhm, A. Dörr, S. Eliseev, S. George, M. Goncharov, Yu. Novikov, J. Repp, S. Sturm, S. Ulmer, and K. Blaum. The trap design of PENTATRAP. Submitted to Appl. Phys. B, 2011.

[Ris11] A. Rischka. Bachelor thesis, Ruprecht-Karls-Universität Heidelberg, 2011. In preparation.

[RMM08] M. Redshaw, J. McDaniel, and E.G. Myers. Dipole Moment of PH^+ and the Atomic Masses of ^{28}Si, ^{31}P by Comparing Cyclotron Frequencies of Two Ions Simultaneously Trapped in a Penning Trap. *Physical Review Letters*, 100(9):93002, 2008.

[ROB+10] J.J. Rabbers, M.P. Oomen, E. Bassani, G. Ripamonti, and G. Giunchi. Magnetic shielding capability of MgB_2 cylinders. *Superconductor Science and Technology*, 23:125003, 2010.

[Ros83] A. Rost. *Grundlagen der Elektronik*. Springer, Wien, New York, 1983.

[Rou11a] C. Roux. PhD thesis, Ruprecht-Karls Universität Heidelberg, 2011. In preparation.

[Rou11b] C. Roux. Private communication, 2011.

[SBN+08] A. Solders, I. Bergström, Sz. Nagy, M. Suhonen, and R. Schuch. Determination of the proton mass from a measurement of the cyclotron frequencies of D^+ and $H_2{}^+$ in a Penning trap. *Physical Review A*, 78:012514, 2008.

[Sho38] W. Shockley. Currents to Conductors Induced by a Moving Point Charge.

Journal of Applied Physics, 9:635–636, 1938.

[Sky08] Skyworks Solutions. *SKY13316-12LF: GaAs IC SPST Non-Reflective Switch 300 kHz–2.5 GHz*, 2008.

[SPS87] T.J. Sumner, J.M. Pendlebury, and K.F. Smith. Conventional magnetic shielding. *Journal of Physics D: Applied Physics*, 20:1095–1101, 1987.

[Sta] www.stahl-electronics.com.

[Sta98] S. Stahl. *Aufbau eines Experimentes zur Bestimmung elektronischer g-Faktoren einzelner wasserstoffähnlicher Ionen.* PhD thesis, Johannes Gutenberg-Universität Mainz, 1998.

[Sta08] Stahl Electronics. *UM 1-14 and UM 1-5 - Multichannel 14V-Range Ultra High Precision Voltage Sources*, 2008.

[Sta10] S. Stahl. *Axialfrequenzverstärker mit integriertem Abwärtsmischer AF-DC-b / AF-DC-c.* Stahl Electronics, 2010.

[Ste68] W.C. Stewart. Current-Voltage Characteristics of Josephson Junctions. *Applied Physics Letters*, 12(8):277–280, 1968.

[SWSB11] S. Sturm, A. Wagner, B. Schabinger, and K. Blaum. A Novel Cyclotron Frequency Measurement Technique at Ultra Low Energies. Submitted to Phys. Rev. Lett., 2011.

[TC77] C.D. Tesche and J. Clarke. dc squid: Noise and Optimization. *Journal of Low Temperature Physics*, 29(3):301–331, 1977.

[Tho97] J.J. Thomson. Cathode Rays. *Philosophical Magazine*, 3:293, 1897.

[Tho07] J.J. Thomson. On Rays of Positive Electricity. *Philosophical Magazine*, 13:561, 1907.

[TS02] U. Tietze and C. Schenk. *Halbleiter-Schaltungstechnik.* Springer, Berlin, Heidelberg, 2002.

[VDS+04] J.L. Verdú, S. Djekić, S. Stahl, T. Valenzuela, M. Vogel, G. Werth, H.J. Kluge, and W. Quint. Determination of the g-Factor of Single Hydrogen-Like Ions by Mode Coupling in a Penning Trap. *Physica Scripta*, 2004:68–72, 2004.

[Ver04] J. Verdú. *Ultrapräzise Messung des elektronischen g-Faktors in wasserstoffähnlichem Sauerstoff.* PhD thesis, Johannes Gutenberg-Universität Mainz, 2004.

[VZV+04] R.S. Van Dyck Jr, S.L. Zafonte, S. Van Liew, D.B. Pinegar, and P.B. Schwinberg. Ultraprecise Atomic Mass Measurement of the α Particle and ^{4}He. *Physical Review Letters*, 92(22):220802, 2004.

[WD75] D.J. Wineland and H.G. Dehmelt. Principles of the stored ion calorimeter. *Journal of Applied Physics*, 46(2):919–930, 1975.

[WLB+88] R.M. Weisskoff, G.P. Lafyatis, K.R. Boyce, E.A. Cornell, R.W. Flanagan, and D.E. Pritchard. rf SQUID detector for single-ion trapping experiments. *Journal of Applied Physics*, 63(9):4599–4604, 1988.

[Wol08] Wolfram Research Inc. *Mathematica, Version 7.0*, 2008.

[ZTH70] J.E. Zimmerman, P. Thiene, and J.T. Harding. Design and Operation of Stable rf-Biased Superconducting Point-Contact Quantum Devices, and a Note on the Properties of Perfectly Clean Metal Contacts. *Journal of Applied Physics*, 41(4):1572–1580, 1970.

Acknowledgements

At this point, I would like to thank some people:

First, I want to thank my first supervisor *Klaus Blaum* for giving me the opportunity to join the PENTATRAP experiment. Thank you for having sparked my interest in Penning traps with your lecture on traps in the first place and for all your advice and support during the thesis.

Thanks to *Christian Roux* for his support at every stage of this thesis. In particular, thank you for the proofreading of most of this thesis. Without your valuable advice, this thesis would not have been the same.

Thanks to *Julia Repp* for the proofreading of the second chapter.

Thanks to *Sergey Elissev*, *Christine Böhm*, *Mikhail Goncharov* and all the other people currently contibuting to the PENTATRAP experiment for creating a positive work atmosphere. Thank you for taking the time to answer my numerous questions and for valuable discussions. I really enjoy working with you.

Thanks to *Stefan Stahl* for his advice concerning the down converter.

Thanks to the "Cryosensors" group at the PTB Berlin and the Magnicon people for their advice concerning the operation of the SQUID.

Thanks to *Christoph Diehl*, *Jochen Ketter*, *Sebastian Streubel* and *Martin Höcker* for being the Penning trap knowledge base in the office right next to mine.

Thanks to *Marius Tremer* for being a great guy to share the office with.

Thanks to *Dominik Keiz* and *Ralph Zilly* for the support in the lab.

Thanks to *Gertraud Dücker* for support in organisational issues.

Thanks to various members of the MPIK staff, who helped wherever they could.

Thanks to *PD Dr. José Crespo* for his willingness to be the second referee of this thesis.

Thanks to my parents for the personal and financial support during the whole time of my studies. Thank you for always believing in me.

Most of all, I want to thank my wonderful wife *Katharina* for supporting me in every possible way, so that I could focus on writing this thesis. Thank you for your patience and your understanding. Thank you for just being there.

Dear Katharina, dear parents, this thesis is dedicated to you.